Geochemical Perspectives Letters

Subsurface particle transport shapes the deep critical zone in a granitoid watershed

X. Gu[1,2*], H. Kim[2,3], S. Hynek[2,4], A. Thompson[5], S.L. Brantley[1,2]

OPEN ACCESS

doi: 10.7185/geochemlet.2127

Abstract

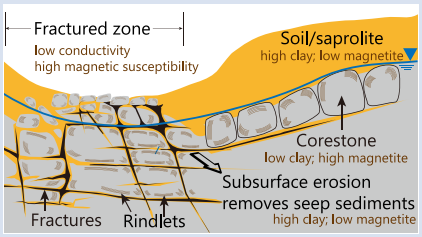

Understanding the inter-relationships between chemical weathering and physical erosion remains a first order puzzle in Earth surface dynamics. In the Río Icacos watershed in the Luquillo Critical Zone Observatory, Puerto Rico, where some of the world's fastest weathering of granitoid watersheds has been measured, we show that chemical weathering not only releases dissolved solutes, but also weakens the rock around the fractures until particles detach and are mobilised by subsurface flow through fractures. These sand-sized particles are more weathered than corestones, but much less weathered than soils/saprolites. Subsurface removal of these clay-enriched, magnetite-depleted particles from the fractures could explain zones with enhanced magnetic susceptibility and decreased terrain conductivity that are observed in geophysical surveys. Subsurface particle transport may thus contribute to geophysical signatures and help sustain high weathering fluxes at Río Icacos and other steep and highly fractured landscapes.

Received 21 March 2021 | Accepted 20 August 2021 | Published 7 October 2021

Introduction

In watershed studies, identification of the input and output components of a mass balance model is the first and the most critical step to quantify fluxes and their importance in the evolution of the critical zone—the layer from the canopy of the trees to the groundwater (Chadwick *et al.*, 1990; Riebe *et al.*, 2017). However, many models are based on incorrect *a priori* assumptions, and end up neglecting important fluxes. For example, most denudation studies are based on the assumption that subsurface losses occur only through the chemical mobilisation of solutes with physical erosion only important for the mobile soil layer (see Riebe *et al.*, 2017 and references therein). However, soil and sediment particles also move below the land surface and even below the soil layer. Subsurface particle transport has been discussed by geomorphologists (*e.g.*, Dunne, 1990), but weathering implications have only been highlighted in a few locations (*e.g.*, Bern *et al.*, 2015; Kim *et al.*, 2018).

To explore the significance of subsurface particle transport in the Luquillo Mountains, Puerto Rico at a site where such transport has been noted (Harrison *et al.*, 2020), we examined "seep sediments" collected from a seep along a steep slope and stream sediments from stream beds in the Río Icacos watershed. As one of the fastest weathering and eroding granitoid systems in the world (White and Blum, 1995), this site has been well studied (White *et al.*, 1998; Buss *et al.*, 2008; Shanley *et al.*, 2011; Comas *et al.*, 2019), allowing us to elucidate how subsurface particle transport contributes to shaping the deep critical zone.

Weathering in the Río Icacos Watershed

The Río Icacos is a bowl-shaped 3.26 km^2 watershed located in the headwaters of the Río Blanco in the Luquillo Mountains of northeastern Puerto Rico (Fig. 1a). This humid, montane tropical forested watershed is almost exclusively developed on the Río Blanco Quartz Diorite, a pluton that contains predominantly plagioclase and quartz (White *et al.*, 1998). In Río Icacos, it has been well documented that spheroidal weathering, initiated by biotite oxidation and volume expansion, fractures to form cm-sized, onion-like rindlets that wrap around increasingly spheroidal corestones (Buss *et al.*, 2008). Each rindlet is characterised by fine microcracks and is separated from other rindlets by larger macro-cracks. The zone of rindlets (~0.5–1 m in thickness) transforms to the thick layer of overlying saprolite and soil. In the following, we first discuss the potential importance of seep sediments and then present evidence for the mechanism of their formation.

Characteristics of Seep and Stream Sediments

Seep sediments were sampled from a perennial seep emanating from between corestones in a roadcut wall along Route 191

1. Department of Geosciences, Pennsylvania State University, University Park, PA 16802, USA
2. Earth and Environmental Systems Institute, Pennsylvania State University, University Park, PA 16802, USA
3. Department of Groundwater and Quaternary Geology Mapping, Geological Survey of Denmark and Greenland, Aarhus 8000, Denmark
4. Utah Water Science Center, USGS, West Valley City, UT 84119, USA
5. Department of Crop and Soil Sciences, University of Georgia, Athens, GA 30602, USA
* Corresponding author (email: xug102@psu.edu)

(Fig. 1b), situated on a steep slope from mountain top to river bottom. The weekly yield of seep sediments produced at the seep during the sampling periods (August–November, 2016) varied by more than one order of magnitude and showed positive correlations with peak discharge and peak rainfall (Fig. 2). The particle size distribution of seep sediments, which varies with discharge (Fig. S-1), is dominated by particles in the upper sand size range (median size: 0.4–1.6 mm). Dissolved Si concentrations in water sampled at the seep during the study measured 375 ± 35 μM, consistent with groundwater that has circulated to tens of metres depth (*cf.* Shanley *et al.*, 2011; Hynek *et al.*, 2017).

Twelve stream sediment samples were collected from beds of the Río Icacos and Quebrada Guaba (an Icacos tributary draining Guaba Ridge, Fig. 1a). The geochemical, mineralogical, and textural signatures indicate the stream sediments are likely mixtures of seep sediments + soils/saprolites. As shown by Buss *et al.* (2008), the composition of the quartz diorite changes as it is transformed first into rindlets, then saprolite, and ultimately soil. Specifically, the extent of depletion in Ca and Na (increasing depletion of plagioclase) increases roughly from corestone to rindlet to seep sediment to stream sediment to soil/saprolite (Fig. 1c). The X-ray diffraction (XRD) patterns and the grain size distributions show the same trends, consistent with weathering extent in these materials (Supplementary Information). Similarly, the concentrations of cosmogenic ^{10}Be in stream sediments at Río Icacos are lower as compared to the soils (Brown *et al.*, 1995; Brocard *et al.*, 2015). These results are consistent with stream sediments in the Río Icacos deriving not only from soils, but also from less weathered materials. These materials were previously assumed to have been delivered by landslides scouring material from depth (Brown *et al.*, 1995; Dosseto *et al.*, 2014). Here, we propose an alternative or additional pathway that these materials are transported as particles through the subsurface.

The characteristics of the seep sediments allow us to constrain the sources of stream sediments at Río Icacos. Assuming that 1) stream sediments are composed of soil/saprolite plus a less weathered component, 2) Al is not solubilised during chemical weathering, and 3) the less weathered component is chemically similar to seep sediments, we estimated 46 ± 22 % and 88 ± 10 % of Na and Ca in the stream sediments at the gages

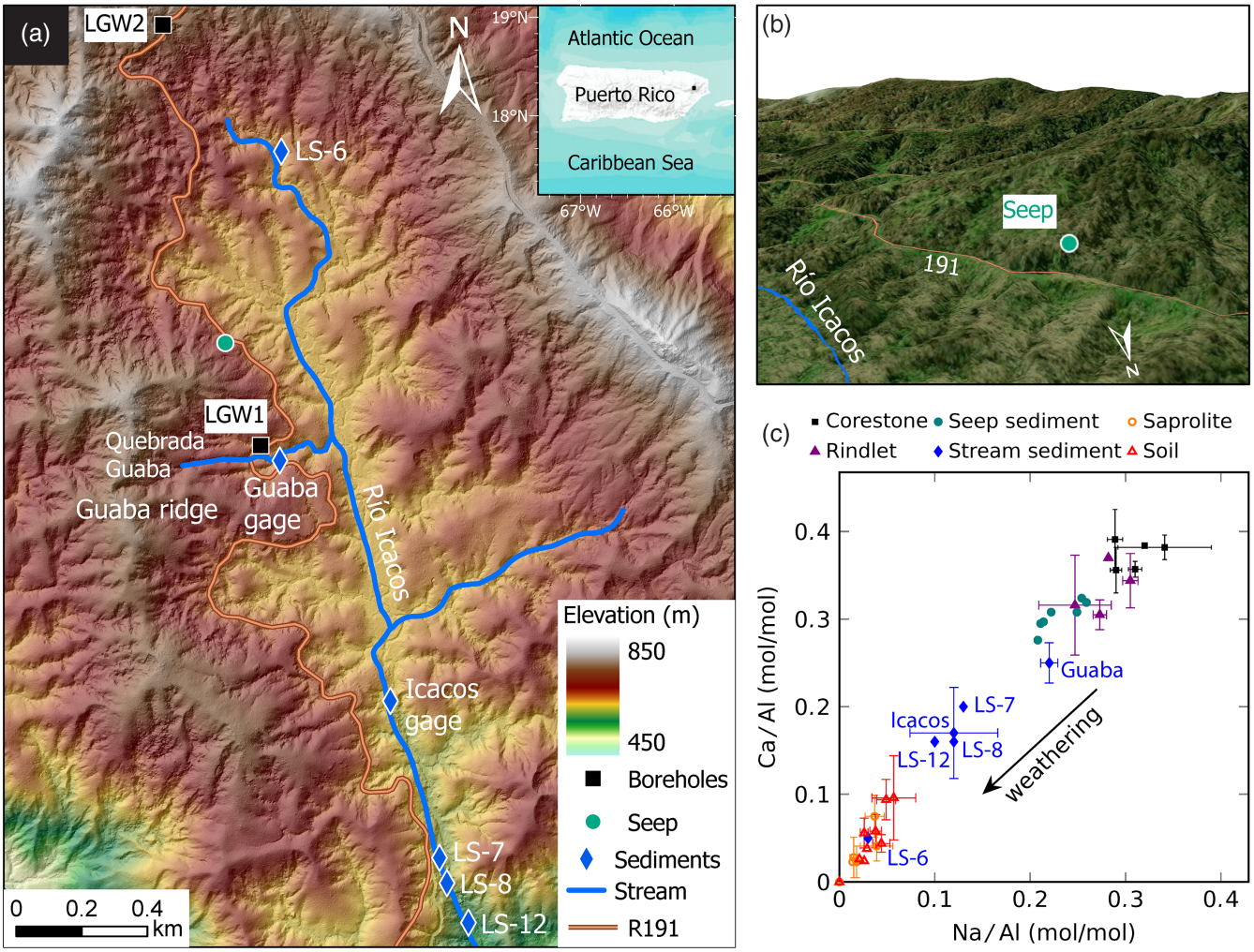

Figure 1 **(a)** Study locations at Río Icacos watershed in Puerto Rico. Colours indicate elevation, which are from USGS 3D Elevation Program through Open Topography. **(b)** Sampling location of seep sediments. Aerial imagery is from Esri (2017). **(c)** Na/Al and Ca/Al molar ratios of different solid end members (corestone, rindlet, seep sediment, stream sediment and saprolite/soil) determined through bulk analysis. Most Na and Ca are present in plagioclase in the bedrock, so as plagioclase weathers, the Na/Al and Ca/Al molar ratios decrease (Al is assumed to be not solubilised during plagioclase weathering).

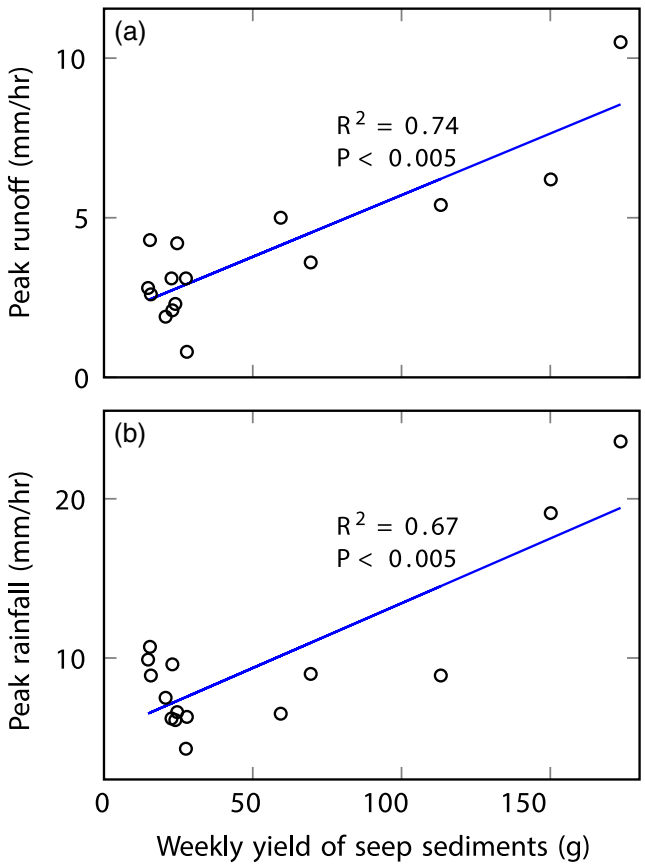

Figure 2 **(a)** Hourly peak runoff and **(b)** maximum rainfall intensity during the sampling week *versus* weekly accumulated mass of seep sediments. P = *p* value.

of Río Icacos and Quebrada Guaba (Fig. 1a), respectively, are sourced from seep sediments or similar less weathered materials (Supplementary Information).

How Subsurface Particle Transport Occurs at Río Icacos

We now consider how such seep sediments might form. In rocks, chemical processes can reduce rock cohesion and enhance the hydraulic conductivity and allow subsurface erosion to occur (Dunne, 1990; Lamb *et al.*, 2006). In the following sections, we summarise observations that document these requirements for subsurface particle transport at Río Icacos: 1) fracture surfaces show enhanced chemical weathering, and 2) the fractured network can support sufficient flow velocities, driven by high hydraulic gradients, to entrain particles.

At Río Icacos, the oxidation of biotite is hypothesised to fracture rock at depth and create fracture-delineated rindlets around the outermost parts of each corestone (*e.g.*, spheroidal weathering; Fletcher *et al.*, 2006; Buss *et al.*, 2008). The textures and compositions of the rindlet interiors are similar to that of the corestones because weathering roughly occurs from outside to inside (Fig. S-2). For example, the degree of alteration of the plagioclase and biotite increases dramatically toward the fracture surface (Fig. 3a–d). Alteration consists of fracturing of the plagioclase as calcic cores become increasingly dissolved or replaced by kaolinite (Fig. 3c). Biotite grains, which become partially to fully altered to vermiculite, increasingly exfoliate parallel to the cleavage plane at the rindlet edges (Fig. 3d). Also, the dissolution of plagioclase (Fig. 3a,c) and exfoliation of biotite (Fig. 3b,d) make these grains easy to detach physically.

Figure 4 exemplifies some of these characteristics. Elemental compositions of plagioclase grains in corestones plot on the mixing line of sodium-rich and calcium-rich plagioclase, showing no chemical weathering (Fig. 4). In contrast, the chemical compositions of plagioclase grains located at the exterior of rindlets span a wide range from unaltered plagioclase to kaolinite and gibbsite, and more than half of the grains are altered. These altered compositions approach that of seep sediments (Fig. 4). We infer that the seep sediments likely originated from the fracture surfaces.

Some of these observations may explain previous geophysical observations at Río Icacos. Ground penetrating radar (GPR) surveys indicated that eroding channels in the hillside leading to the river are usually co-located with vertical zones of enhanced GPR reflection. These were interpreted as deep fracture zones filled with rindletted corestones (Comas *et al.*, 2019). Field measurements across these fracture zones showed coincident decreases in terrain conductivity and increases in magnetic susceptibility (Comas *et al.*, 2019). To test what might cause this, we conducted magnetic susceptibility (MS) measurements in the laboratory and observed that the MS values decreased from corestones ≈ rindlets > seep sediments > soils (Table S-1). The decrease of MS is likely due to depletion of magnetite during weathering as documented by XRD (Supplementary Information); these measurements also showed that clay minerals (known to generally show relatively high electrical conductivity, EC (Palacky, 1987)) are enriched in seep sediments (Table S-2). These new data therefore show that the low EC in fracture zones could be caused by loss of particles like the clay-rich seep sediments while the high MS could be caused by retention of magnetite in the corestones and rindlets as seep sediment-like particles are removed.

Another geomorphological characteristic, amphitheatre-shaped headwalls throughout the Río Icacos, provides additional evidence of seepage erosion (Harrison *et al.*, 2020). For example, the steep slopes of headwalls around the sampled seep (27–60°) should provide a sufficient hydraulic gradient for subsurface particle flow. Hydrologic calculations also suggest that the size of fracture apertures is large enough to accommodate the size of seep sediments (Supplementary Information). In fact, during drilling in the quartz diorite, movement of particles in the subsurface between boreholes separated by 1 m has even been noted (Orlando, 2014).

Fracture Surfaces are Hot Spots for Weathering and Erosion

The chemical weathering rate of silicates as indicated by the riverine flux at Río Icacos is among the highest reported for granitoid watersheds (White and Blum, 1995). However, the high weathering rate at Río Icacos cannot be fully explained by the humid tropical climate since the rate is 4 to 20 times higher than other granitoid watersheds in tropical areas with high precipitation (Edmond *et al.*, 1995; von Blanckenburg *et al.*, 2004; Braun *et al.*, 2012). The high weathering flux at Río Icacos has previously been attributed to the interconnected fractures that allow fast infiltration of oxygenated meteoric water that can accelerate weathering at multiple depths (*e.g.*, Fletcher *et al.*, 2006). Our study suggests that the transport of sand-sized particles through fractures at Río Icacos is an under-appreciated mechanism that exposes fresh particle surfaces to weathering fluids. Subsurface particle transport has not been previously invoked to explain the 10 fold discrepancies between short term denudation rates

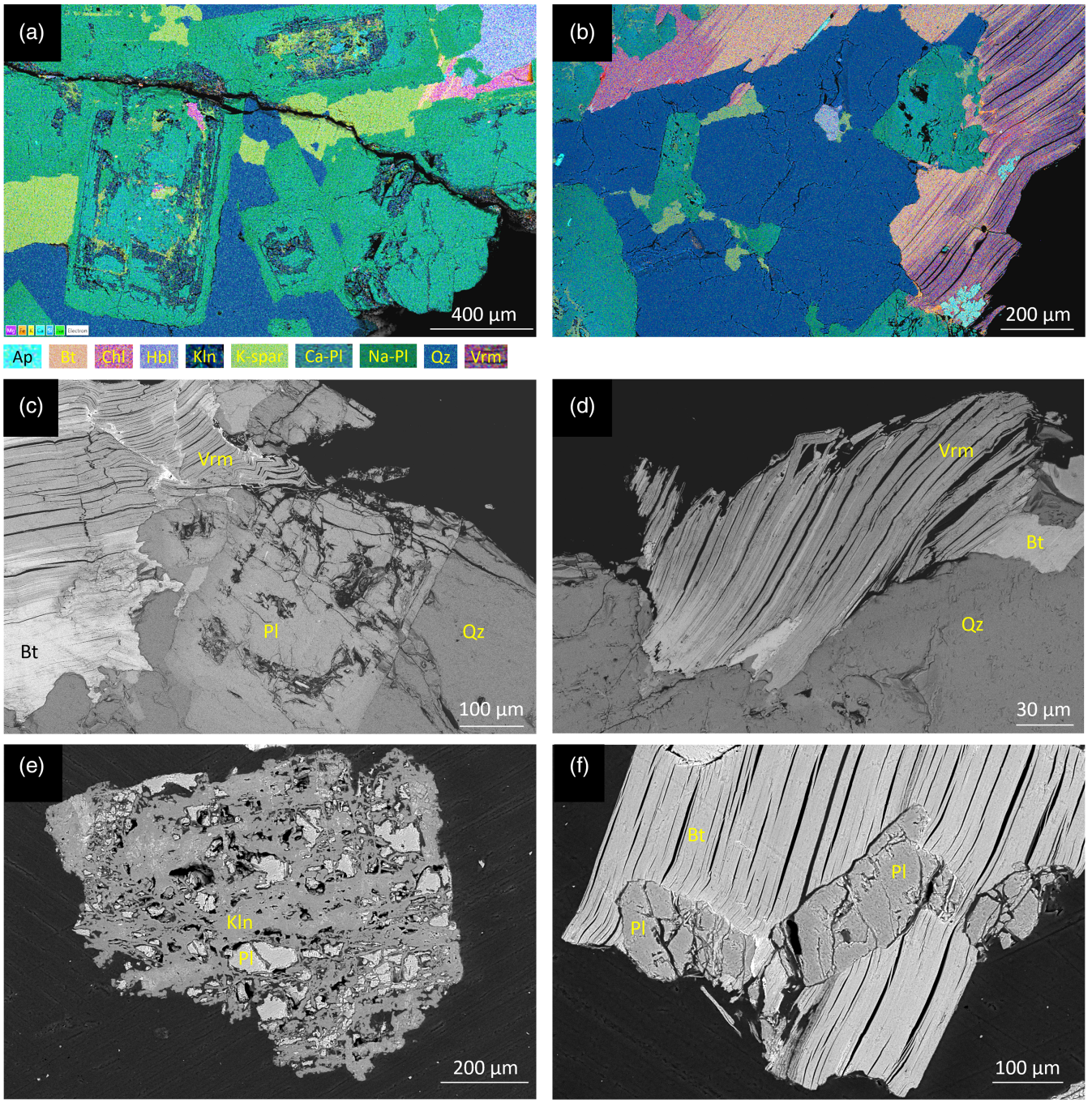

Figure 3 **(a, b)** Elemental maps and **(c–f)** backscattered electron images of the edge of rindlets **(a–d)** and seep sediments **(e, f)**. The rindlet sample is from borehole LGW1 at 5.38–5.40 metres below land surface (LGW1 1-20) and the seep sediments were collected during August 9–16, 2016 (0.85–2.56 mm size fraction). Ap: apatite, Bt: biotite, Chl: chlorite, Hbl: hornblende, Kln: kaolinite, K-spar: K-feldspar, Pl: plagioclase, Qz: quartz, Vrm: vermiculite.

inferred from solid loads at stream gages (Stallard, 2012) and the long term denudation rates inferred from cosmogenic ^{10}Be (Brown *et al.*, 1995). The stream sediments of Río Icacos are enriched in cosmogenic ^{10}Be from soils, but also contain seep sediments that do not contain ^{10}Be due to delivery from depth. Whether this means that denudation rates are underestimated remains to be explored.

Chemical weathering in fractured rocks has been relatively well studied. However, our understanding of particle transport through fractures is very limited because it is based on only a few studies such as those in carbonate (Levenson and Emmanuel, 2017) or carbonate-rich shale lithologies (Deng *et al.*, 2017). The significance of subsurface particle transport depends on disaggregation related to weathering of the fracture surface, the size of the particles relative to the fracture apertures, the fracture connectivity, and the hydraulic gradient. Subsurface particle transport is an under-appreciated process that likely shapes the deep critical zone and promotes chemical and physical weathering in mountainous areas with well developed fracture networks like the Luquillo Mountains. More investigations are needed to characterise particle transport by subsurface flow through different fracture geometries, in different lithologies, and at different temporal and spatial scales.

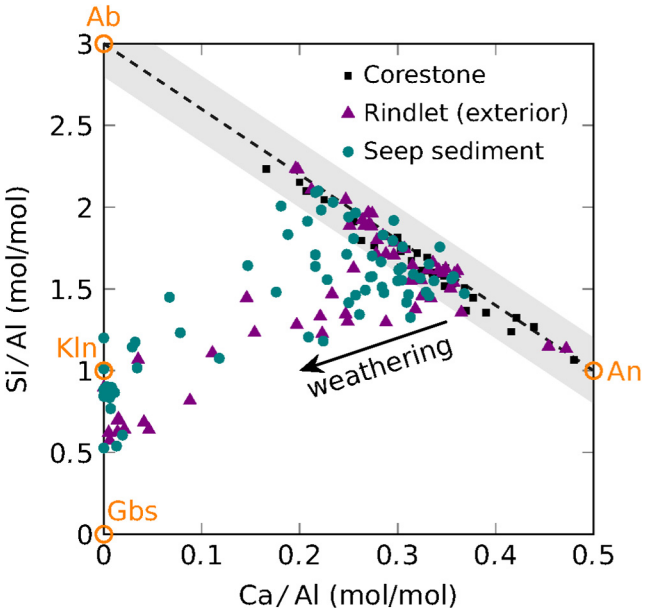

Figure 4 Si/Al and Ca/Al molar ratios determined by scanning electron microscopy energy dispersive X-ray spectroscopy (EDS) on individual plagioclase grains from different solid end members (corestone, rindlet and seep sediment). The orange circles represent sodium-rich (albite, Ab) and calcium-rich (anorthite, An) plagioclase and typical weathering products of plagioclase such as gibbsite (Gbs) and kaolinite (Kln). The dashed line represents solid solution mixing of Ab and An. Shaded zone shows one standard deviation of uncertainty in Ca/Al molar ratios assuming the relative error of EDS measurement is 5 %. Therefore, the points within the shaded zone are considered as unaltered plagioclase.

Acknowledgements

We thank technical support from the Materials Characterization Laboratory and Laboratory for Isotopes and Metals in the Environment at the Pennsylvania State University. We thank Jean-Marc Baele and an anonymous reviewer for helpful comments. This work was funded by the National Science Foundation Luquillo Critical Zone Observatory (NSF-LCZO), Grant EAR 1331841 to Bill McDowell.

Editor: Sophie Opfergelt

Additional Information

Supplementary Information accompanies this letter at https://www.geochemicalperspectivesletters.org/article2127.

Cite this letter as: Gu, X., Kim, H., Hynek, S., Thompson, A., Brantley, S.L. (2021) Subsurface particle transport shapes the deep critical zone in a granitoid watershed. *Geochem. Persp. Let.* 19, 13–18.

References

Bern, C.R., Thompson, A., Chadwick, O.A. (2015) Quantification of colloidal and aqueous element transfer in soils: The dual-phase mass balance model. *Geochimica et Cosmochimica Acta* 151, 1–18.

Braun, J.-J., Marechal, J.-C., Riotte, J., Boeglin, J.-L., Bedimo Bedimo, J.-P., Ndam Ngoupayou, J.R., Nyeck, B., Robain, H., Sekhar, M., Audry, S., Viers, J. (2012) Elemental weathering fluxes and saprolite production rate in a Central African lateritic terrain (Nsimi, South Cameroon). *Geochimica et Cosmochimica Acta* 99, 243–270.

Brocard, G.Y., Willenbring, J.K., Scatena, F.N., Johnson, A.H. (2015) Effects of a tectonically-triggered wave of incision on riverine exports and soil mineralogy in the Luquillo Mountains of Puerto Rico. *Applied Geochemistry* 63, 586–598.

Brown, E.T., Stallard, R.F., Larsen, M.C., Raisbeck, G.M., Yiou, F. (1995) Denudation rates determined from the accumulation of in situ-produced ^{10}Be in the Luquillo Experimental Forest, Puerto Rico. *Earth and Planetary Science Letters* 129, 193–202.

Buss, H.L., Sak, P.B., Webb, S.M., Brantley, S.L. (2008) Weathering of the Rio Blanco quartz diorite, Luquillo Mountains, Puerto Rico: Coupling oxidation, dissolution, and fracturing. *Geochimica et Cosmochimica Acta* 72, 4488–4507.

Chadwick, O.A., Brimhall, G.H., Hendricks, D.M. (1990) From a black to a gray box – a mass balance interpretation of pedogenesis. *Geomorphology* 3, 369–390.

Comas, X., Wright, W., Hynek, S.A., Fletcher, R.C., Brantley, S.L. (2019) Understanding fracture distribution and its relation to knickpoint evolution in the Rio Icacos watershed (Luquillo Critical Zone Observatory, Puerto Rico) using landscape-scale hydrogeophysics. *Earth Surface Processes and Landforms* 44, 877–885.

Deng, H., Voltolini, M., Molins, S., Steefel, C., DePaolo, D., Ajo-Franklin, J., Yang, L. (2017) Alteration and erosion of rock matrix bordering a carbonate-rich shale fracture. *Environmental Science & Technology* 51, 8861–8868.

Dosseto, A., Buss, H.L., Chabaux, F. (2014) Age and weathering rate of sediments in small catchments: The role of hillslope erosion. *Geochimica et Cosmochimica Acta* 132, 238–258.

Dunne, T. (1990) Hydrology mechanics, and geomorphic implications of erosion by subsurface flow. In: Higgins, C.G., Coates, D.R. (Eds.) *Groundwater geomorphology: The role of subsurface water in Earth-surface processes and landforms*. Geological Society of America, Boulder, 1–28.

Edmond, J.M., Palmer, M.R., Measures, C.I., Grant, B., Stallard, R.F. (1995) The fluvial geochemistry and denudation rate of the Guayana Shield in Venezuela, Colombia, and Brazil. *Geochimica et Cosmochimica Acta* 59, 3301–3325.

Esri (2017) "World Imagery" [imagery]. 1:6,700 scale. "World Imagery". October 24, 2017. https://www.arcgis.com/home/item.html?id=10df2279f9684e4a9f6a7f08febac2a9. (September 16, 2021).

Fletcher, R.C., Buss, H.L., Brantley, S.L. (2006) A spheroidal weathering model coupling porewater chemistry to soil thicknesses during steady-state denudation. *Earth and Planetary Science Letters* 244, 444–457.

Harrison, E.J., Brocard, G.Y., Gasparini, N.M., Lyons, N.J., Willenbring, J.K. (2020) Seepage erosion in the Luquillo Mountains, Puerto Rico, relict landscapes. *Journal of Geophysical Research: Earth Surface* 125, e2019JF005341.

Hynek, S., Comas, X., Brantley, S.L. (2017) The effect of fractures on weathering of igneous and volcaniclastic sedimentary rocks in the Puerto Rican tropical rain forest. *15th Water-rock Interaction International Symposium*, Wri-15. 972–975.

Kim, H., Gu, X., Brantley, S.L. (2018) Particle fluxes in groundwater change subsurface shale rock chemistry over geologic time. *Earth and Planetary Science Letters* 500, 180–191.

Lamb, M.P., Howard, A.D., Johnson, J., Whipple, K.X., Dietrich, W.E., Perron, J.T. (2006) Can springs cut canyons into rock? *Journal of Geophysical Research: Planets* 111, E07002.

Levenson, Y., Emmanuel, S. (2017) Repulsion between calcite crystals and grain detachment during water-rock interaction. *Geochemical Perspectives Letters* 3, 133–141.

Orlando, J. (2014) The anatomy of weathering profiles on different lithologies in the tropical forest of northeastern Puerto Rico: from bedrock to clouds. Master thesis: Pennsylvania State University.

Palacky, G.J. (1987) Resistivity characteristics of geologic targets. In: Nabighian, M.N. (Ed.) *Electromagnetic Methods in Applied Geophysics*. Society of Exploration Geophysicists, Tulsa, 52–129.

Riebe, C.S., Hahm, W.J., Brantley, S.L. (2017) Controls on deep critical zone architecture: a historical review and four testable hypotheses. *Earth Surface Processes and Landforms* 42, 128–156.

Shanley, J.B., McDowell, W.H., Stallard, R.F. (2011) Long-term patterns and short-term dynamics of stream solutes and suspended sediment in a rapidly weathering tropical watersheds. *Water Resources Research* 47, W07515.

Stallard, R.F. (2012) Weathering, landscape equilibrium, and carbon in four watersheds in eastern Puerto Rico. USGS Professional Paper 1789-H.

von Blanckenburg, F., Hewawasam, T., Kubik, P.W. (2004) Cosmogenic nuclide evidence for low weathering and denudation in the wet, tropical highlands of Sri Lanka. *Journal of Geophysical Research: Earth Surface* 109, F03008.

White, A.F., Blum, A.E. (1995) Effects of climate on chemical weathering in watersheds. *Geochimica et Cosmochimica Acta* 59, 1729–1747.

White, A.F., Blum, A.E., Schulz, M.S., Vivit, D.V., Stonestrom, D.A., Larsen, M., Murphy, S.F., Eberl, D. (1998) Chemical weathering in a tropical watershed, Luquillo mountains, Puerto Rico: I. Long-term versus short-term weathering fluxes. *Geochimica et Cosmochimica Acta* 62, 209–226.

Geochemical Perspectives Letters

Subsurface particle transport shapes the deep critical zone in a granitoid watershed

X. Gu, H. Kim, S. Hynek, A. Thompson, S.L. Brantley

Supplementary Information

The Supplementary Information includes:

- Full Description of the Study Site and Sampling Protocols
- Analytical Methods
- Water Sampling and Analysis
- XRD Patterns
- Grain Size of Soils, Stream and Seep Sediments
- Characteristics of Fracture
- Quantifying the End Members of Stream Sediments
- Tables S-1 to S-6
- Figures S-1 to S-7
- Supplementary Information References

Full Description of the Study Site and Sampling Protocols

The Río Icacos watershed is located in the Luquillo Mountains of northeastern Puerto Rico. It's hot and humid climate (with mean annual air temperature of 22 °C and mean annual precipitation of 4200 mm, White *et al*., 1998) results in dense, tropical vegetation. The steep relief varies from 620 to 832 m in elevation. The Río Icacos, a tributary of the Río Blanco, flows north to south in its watershed with an average channel gradient of ~0.9 % (Orlando *et al*., 2016).
The Río Icacos watershed is almost exclusively developed on Río Blanco Quartz Diorite, an igneous pluton that contains predominantly plagioclase (50–60 %) and quartz (20–30 %) with lesser amounts of biotite and hornblende, and accessory magnetite, K-feldspar, sphene, ilmenite, apatite, and zircon (White *et al*., 1998; Turner *et al*., 2003; Buss *et al*., 2008). The bedrock is now classified as a tonalite according to the current IUGS classification scheme (Buss *et al*., 2017) but has been referred to as a quartz diorite repeatedly in the literature. In the (unweathered) corestones, plagioclase grains are 0.2–2 mm in size, and typically contain calcic cores with more sodic rims (Fig. S-2a, b). Biotite grains are similar in size as the plagioclase, and the edges are replaced by chlorite in some cases (Fig. S-2d). Magnetite is present as exsolved inclusions within silicates, and as coarse grains (Fig. S-2a, c, d).

Research in the Río Icacos watershed has been supported by several long-term observatory programs as part of the US Forest Service Luquillo Experimental Forest (LEF), the US Geological Survey Water Energy and Biogeochemical Budgets (WEBB) program, the National Science Foundation (NSF) Long Term Ecological Research (LTER) and NSF Luquillo Critical Zone Observatory (LCZO). The patterns, rates and mechanisms of chemical weathering of quartz diorite at the Río Icacos watershed have been well documented (White *et al*., 1998; Murphy *et al*., 1998; Riebe *et al*., 2003; Turner *et al*., 2003; Buss *et al*., 2008; Ferrier *et al*., 2010; Brantley *et al*., 2011; Chabaux *et al*., 2013; Brocard *et al*., 2015; Hynek *et al*., 2017), and the chemical characterisation of the solid end members with respect to weathering have been well constrained. Geochemical weathering models for the system are consistent with the following sequence of reactions in the system: i) biotite oxidises in intact corestones (Buss *et al*., 2008); ii) slight volume expansion causes spheroidal fracturing (Fletcher *et al*., 2006); iii) micro-cracking of the rindlets enhances dissolution of feldspar and hornblende (Navarre-Sitchler *et al*., 2013); iv) rindlets increasingly transform to saprolitic material outboard from the corestone; v) eventually rindlets disappear and are completely replaced by saprolite. The quartz-rich soil is generally about one meter thick, but the underlying saprolite varies in thickness from meters to tens of meters (Buss *et al*., 2008; Orlando *et al*., 2016).

In the roadcut along Route 191 that parallels the upper Río Icacos, corestones can be seen in cross-section, stacked one on top of one another with rindlets and saprolite in between (Orlando *et al*., 2016). Fracture zones cross the road sub-perpendicularly, carrying water from higher elevations to the river. The density of these fracture zones increases down-elevation toward the knickpoint (Fletcher *et al*., 2006; Comas *et al*., 2019).

To sample seep sediments, a perforated bucket with a filter bag (100 µm filter size) was placed under the perennial seep between corestones in a road cut wall along Route 191 (Fig. S-3). The bag was recovered every week. Stream sediments (~1 kg at each site) were collected from stream beds across the channel over a channel length of ~10–20 m. The stream sediments at the gages of Río Icacos and Quebrada Guaba were sampled several times. The soils were sampled from Guaba Ridge close to the soil pits reported in White *et al*. (1998). The soil, seep and stream sediment samples were dried at room temperature and then kept in a plastic bag until analysis. The air-dried samples were sieved using stainless steel sieves at 0.1–0.25 mm, 0.25–0.42 mm, 0.42–0.85 mm, 0.85–2.56 mm and > 2.56 mm size fractions (Table S-3).

Analytical Methods

All solid samples were air-dried, split and pulverised using a ceramic mortar and pestle to less than 150 µm. The pulverised aliquot (100 mg) was analysed by inductively coupled plasma-atomic emission spectroscopy (ICP-AES; Perkin-Elmer Optima 5300DV ICP-AES) after Li metaborate fusion digestion at the Laboratory for Isotopes and Metals in the Environment (LIME) at the Pennsylvania State University (Table S-4).

X-ray diffraction (XRD) was performed on pulverised aliquots using a Malvern Panalytical Empyrean II X-Ray Diffractometer with a Co $K\alpha$ radiation at 45 kV and 40 mA, in a rate of 4° min^{-1} from 5.8° to 84° 2θ in the Bragg-Bentano configuration at Material Characterization Laboratory (MCL) at the Pennsylvania State University. Divergence and antiscatter slits of 1/8 and 1/2° were used together with a 0.04 rad soller slit in the incident beam optics. A 0.04 rad soller slit and antiscatter slits of 1/4° were used in the diffracted optics. Mineral abundances were semi-quantified by RockJock (Eberl, 2003).

For microscopic analysis, selected corestones, rindlets and seep sediments were impregnated with clear, very low viscosity epoxy (Buehler Epothin 2) and cut into thin sections. The thin sections were polished, coated with carbon (~5 nm in thickens) and imaged in backscattered electron (BSE) mode by a Thermo Scientific Q250 scanning electron microscopy (SEM) at MCL at the Pennsylvania State University (Figs. 3, S-2, S-4). Mineral identification and composition were determined based on energy dispersive spectrometry (EDS, Oxford Silicon Drift Detector) data

collected at an accelerating voltage of 20 kV and system dead times of 25–50 %. The elemental concentrations of plagioclase grains and the weathering byproducts were semi-quantified using the Oxford Instruments AZtec acquisition and analysis software (Table S-5).

Mass-specific magnetic susceptibility measurements were collected on pulverised aliquots on a Bartington MS3 magnetic susceptibility meter with a MS2B Dual Frequency Sensor. Measurements were made in low frequency mode and cross calibrated with an in-house set of soil standards (Thompson *et al*., 2011) before each analytical session.

Water Sampling and Analysis

Water samples were collected and filtered (0.45 µm filter) at the seep and the Quebrada Guaba gage from 2012–2016. Major cations and dissolved silica were analysed by ICP-AES after acidified by nitric acid. Anions were measured on a Dionex Ion Chromatograph (ICS-250; Sunnyvale, California). All measurement were conducted at LIME at the Pennsylvania State University.

The concentrations of Si in seep water (375 ± 35 µM, Table S-6) are slightly lower than the values of stream base flow at Río Icacos (450 ± 13 µM), which are assumed to represent the deep groundwater (Shanley *et al*., 2011), and much higher than the shallow groundwater (75–129 µM, McDowell *et al*., 1992) and soil water (53–216 µM, White *et al*., 1998). The elevated concentrations of Si, primarily derived from silicates weathering at depth (Bhatt and McDowell, 2007), indicates that the seep may source from ~20 m deep from the land surface (Hynek *et al*., 2017). Similarly, elevated Si concentrations in stream water of Quebrada Guaba (233 ± 56 µM), drained from highly fractured Guaba Ridge, indicate the stream is largely fed by groundwater.

XRD Patterns

The XRD patterns also show distinctive signatures in different solid endmembers at Río Icacos. The bulk mineralogy of the rindlets and corestones mainly includes plagioclase, biotite, quartz, and hornblende as major minerals, and apatite, chlorite, magnetite, and sphene as minor phases (Fig. S-5). Each rindlet and corestone sample shows small variations in mineral abundance. Similar variations were observed in elemental compositions (Table S-4). Biotite is completely depleted in all seep sediment samples, and plagioclase, hornblende, and chlorite are mostly depleted as compared to corestones (Fig. S-6). Plagioclase, and hornblende are more enriched in the bigger particles (*e.g.*, > 0.85 mm) than in the smaller particles, while vermiculite, the weathering product of biotite (Murphy *et al*., 1998), is enriched in the smaller particles (Fig. S-6). Only quartz (the most weathering-resistant major mineral at Río Icacos), kaolinite, and gibbsite (produced from plagioclase and biotite weathering) and vermiculite (produced from biotite weathering) were detected in soils (Fig. S-7). Similar to the elemental results (Fig. 1c), the XRD pattern of stream sediments shows mineral compositions lie between that of the seep sediments and the soils (Fig. S-7). The partially depletion of magnetite in seep sediments and completely depletion in soils as compare to corestones is consistent the values of magnetic susceptibility measured in these samples (Table S-1).

The preferred orientation (partly due to large particle size of primary minerals) made the semi-quantification difficult for less-weathered samples (*e.g.*, corestones and rindlets), so we only reported the results for soils, seep and stream sediments (Table S-2). It is clear that coarser fractions of seep sediments are less weathered since the abundance of primary silicates (plagioclase and hornblende) are higher and the abundance of secondary clay minerals (kaolinite and vermiculite) are lower in coarser fractions. The abundance of quartz is higher in finer fractions of seep sediments, likely due to the preferential removal of secondary clay minerals through hydraulic sorting. The abundance of primary silicates is higher in stream sediments than in soils. The abundance of quartz is similar in soils (62–78 wt. %) as in stream sediments (62–70 wt. %), and both are close to the reported values in soils at Río Icacos (49–82 wt. %, Schulz and White, 1999; Ferrier *et al*., 2010; Brocard *et al*., 2015).

Grain Size of Soils, Stream and Seep Sediments

The median particle size (D_{50}) of stream sediments (0.40–0.66 mm) is close to the value of stream sediments collected at the gage at Río Icacos (~0.51 mm, Saraceno *et al*., 2017). The D_{50} of seep sediments spans a wide range from 0.35 to 1.6 mm (Table S-3). Most grains in soils are smaller than medium sand size (D_{50}: 0.13–0.18 mm), and no grains larger than 0.85 mm were observed. These results are consistent with the elemental and mineralogical interpretation that stream sediments are mixtures of soils and less weathered materials with larger grain size such as seep sediments.

Characteristics of Fracture

Near surface geophysical surveys and observations from outcrops along Route 191 have revealed that the fracturing zones are mainly located in valley areas that drain to Rio Icacos (Orlando *et al*., 2016; Comas *et al*., 2019). Estimated through GPR profiles, the horizontal widths and vertical depths of the fracturing zones are roughly 10–60 m and 5–20 m, respectively. Some large voids were encountered during drilling at Rio Icacos as evidenced by 1) the drill bit dropped so rapidly at times that the drillers were confident in identifying certain regions in the subsurface as voids; 2) a piece of cement for PVC casing for one borehole was recovered in another borehole one meter away; 3) drilling fluids were lost rapidly at a rate of 4–20 gallons per minute (Orlando, 2014).

The highly fractured network results in high hydraulic conductivity in the subsurface at Rio Icacos. The bulk hydraulic conductivity measured in borehole LGW2B (total depth: 25.3 m, water table: 15–16 meters below land surface, mbls) by pumping test is (0.7–2.8) × 10^{-5} m s^{-1} (Orlando, 2014), which is within the range of fractured igneous and metamorphic rock (Freeze and Cherry, 1979). We further estimated equivalent hydraulic aperture of fractures (b) on the basis of the cubic law (Snow, 1969) assuming 1) the conductivity of rock matrix between fractures is negligible and 2) the fractures are subparallel as observed in outcrops and cores:

$$b = [12K_bB\mu/\rho g]^{1/3} \quad \text{(Eq. S-1)}$$

where K_b is bulk hydraulic conductivity, B is fracture spacing (reciprocal of fracture density), μ is dynamic viscosity of water, μ is density of water and g is acceleration of gravity. Based on the bulk hydraulic conductivity measured in borehole LGW2B and fracture density measured in five boreholes at Rio Icacos (0.2–1 fracture m^{-1}), the equivalent hydraulic aperture of fractures is calculated to be 0.20–0.56 mm. Since the physical aperture of fractures is usually at the same magnitude but larger than the equivalent hydraulic aperture of fractures due to roughness of fracture surface (Brown, 1987), the hydrologic parameters suggest the aperture of fractures in the subsurface at Rio Icacos is probably large enough to allow particle transport (d_{50} of seep sediments is 0.59 ± 0.33 mm, Table S-3).

Quantifying the End Members of Stream Sediments

Multiple evidences have shown the stream sediments are consist of two endmembers: 1) soils/saprolite and 2) less weathered materials (see main text). The less weathered materials could be sourced from mechanical weathering in subsurface (particles transported by seep as we discussed here) or from corestones that crop out at the surface or from landslides. Here we use the ratios of Na/Al and Ca/Al as indicator of chemical weathering of plagioclase, since Al is almost completely immobile during chemical weathering (notice the low concentrations of Al in seep and stream water, Table S-6). It is clear that the ratios of Na/Al and Ca/Al of most of the stream sediments lie between seep sediments and soils/saprolites (Fig. 1c). We calculated the fraction of the two endmembers in stream sediments with respect to Na and Ca using the equations below:

$$\alpha_1(c_{j,1}/c_{i,1}) + \alpha_2(c_{j,2}/c_{i,2}) = c_{j,sed}/c_{i,sed} \quad \text{(Eq. S-2)}$$

$$\alpha_1 + \alpha_2 = 1 \qquad \text{(Eq. S-3)}$$

where α_1 and α_2 are the fraction of end member 1 (soils/saprolite) and end member 2 (less weathered materials) in stream sediments, respectively. c_j is the concentration of mobile elements (here Ca and Na) and c_i is the concentration of immobile elements (here Al). We obtained $\alpha_2 = 0.80 \pm 0.10$ (using Ca) or 0.95 ± 0.11 (using Na) for sediments collected at the Quebrada Guaba gage and $\alpha_2 = 0.50 \pm 0.21$ (using Ca) or 0.43 ± 0.24 (using Na) for sediments collected at the Río Icacos gage.

Supplementary Tables

Table S-1 Magnetic susceptibility (MS, 10^{-8} m^3 kg^{-1}) results of different solid samples at Río Icacos watershed.

Sample type	Sample ID	MS
Soil	Guaba Soil 1	8
Seep sediment	Collected 8/9–8/16/2016, > 2.56 mm fraction	827
	Collected 8/9–8/16/2016, 0.85–2.56 mm fraction	975
	Collected 8/9–8/16/2016, 0.42–0.85 mm fraction	1231
	Collected 8/9–8/16/2016, 0.25–0.42 mm fraction	1096
	Collected 8/9–8/16/2016, 0.1–0.25 mm fraction	1044
	Collected 11/8–11/15/2016, > 2.56 mm fraction	424
	Collected 11/8–11/15/2016, 0.85–2.56 mm fraction	827
	Collected 11/8–11/15/2016, 0.42–0.85 mm fraction	751
	Collected 11/8–11/15/2016, 0.25–0.42 mm fraction	835
Rindlet	LCZO 3-8 (Chabaux *et al*., 2013)	1810
	LCZO RC-5 (Chabaux *et al*., 2013)	2143
	LCZO RC-1 (Chabaux *et al*., 2013)	1969
Corestone	LGW1 16-2 (Orlando, 2014)	1581
	LGW2 20-RBZ (Orlando, 2014)	1935

Table S-2 Mineralogy of soils, stream and seep sediments at Río Icacos (weight percent, normalised to 100, determined using RockJock).

Sample type	Sample ID	Quartz	Plagioclase	Hornblende	Biotite	Kaolinite	Vermiculite	Gibbsite	Fe and Ti oxides [1]
Soil	Rio_Iccos_soil	78	7	3	1	10	2	0	0
	Guaba Soil 1	70	1	0	0	23	0	3	2
	Guaba Soil 2	62	3	1	1	20	4	7	2
Stream sediments	LS-9	69	7	2	0	12	10	0	0
	LS-5	70	14	6	2	7	1	0	1
	LS-2	62	19	5	2	9	2	1	1
Seep sediments collected during August-02 to August-07, 2016	ICZOs-6 (0.1–0.25 mm)	62	2	1	0	25	7	0	3
	ICZOs-7 (0.25–0.42 mm)	58	16	1	1	14	8	0	3
	ICZOs-8 (0.42–0.85 mm)	46	16	3	1	13	19	0	1
	ICZOs-9 (0.85–2.56 mm)	35	23	4	0	10	26	0	2
	ICZOs-10 (> 2.56 mm)	20	52	6	0	8	13	0	1

[1] Including magnetite, haematite, goethite and ilmenite.

Table S-3 Particle size fractions of seep sediments, stream sediments and soils collected at Río Icacos watershed.

	Site/Collection time	Peak runoff (mm/hr) [1]	Peak rainfall (mm/hr) [2]	Particle size fractions (in g)						D_{50} (um)
				0.1-0.25 mm	0.25-0.42 mm	0.42-0.85 mm	0.85-2.56 mm	> 2.56 mm	Total	
Seep sediments	7/26/2016–8/2/2016	3.1	6.2	1.81	1.81	2.31	5.85	10.91	22.69	1623
	8/2/2016–8/9/2016	5.0	6.5	8.09	8.24	8.02	16.05	19	59.4	925
	8/9/2016–8/16/2016	5.4	8.9	14.88	22.08	22.09	32.08	22.07	113.2	591
	8/16/2016–8/26/2016	0.8	6.3	3.09	2.92	4.19	9.89	7.77	27.86	961
	8/26/2016–9/2/2016	3.6	9.0	12.15	17.06	17.84	13.26	9.17	69.48	407
	9/2/2016–9/6/2016	2.6	8.9	2.92	3.9	4.33	4.33	0.28	15.76	395
	9/6/2016–9/13/2016	2.1	9.6	5.19	3.49	6.14	6.7	1.46	22.98	459
	9/13/2016–9/20/2016	1.9	7.5	4.4	5.62	4.72	4.91	1.06	20.71	351
	9/20/2016–9/27/2016	4.3	10.7	3.76	3.42	2.57	3.59	2.11	15.45	382
	9/27/2016–10/4/2016	2.8	9.9	2.26	4.08	3.69	4.04	0.75	14.82	403
	10/4/2016–10/11/2016	4.2	6.6	3.73	6.81	6.94	5.59	1.53	24.6	394
	10/18/2016–10/25/2016	2.3	6.1	4.49	6.02	6.2	6.89	0.38	23.98	393
	10/26/2016–11/1/2016	3.1	4.3	5.82	7.04	6.32	6.91	1.45	27.54	368
	11/1/2016–11/8/2016	6.2	19.1	14.18	32.14	59.41	40.2	4.23	150.16	458
	11/8/2016–11/15/2016	10.5	23.6	5.77	10.8	84.96	61.74	10.35	173.62	565
Stream sediments	Rio Icacos gage (02/25/2014)			12.09	24.37	36.35	14.79	2.84	12.09	395
	LS-3 Guaba gage (03/02/2014)			5.95	11.01	18.66	24.84	13.26	5.95	664
	LS-7			1.87	13.29	40.25	21.06	4.26	1.87	495
Soils	Icacos soil			16.42	7.24	2.35	0	0	25.98	184
	Guaba soil 1			10.56	8.76	3.28	0	0	22.83	127
	Guaba soil 2			14.53	10.38	4.5	0	0	29.68	125

[1] Data are from USGS gage station 50075000.

[2] Precipitation data are available at the USGS gage station 50075000 from 2016-10-01. The data before 2016-10-01 are from a nearby meteorological station. The description of the station and the data are available at: https://www.sas.upenn.edu/lczodata/content/east-peak-iitf-climate-station.

Table S-4 Summary of elemental concentrations of bulk samples at Río Icacos watershed (wt. %, except ppm for Zr, reported as-received basis).

Type	Sample/Sources	Lat	Lon	Al	Ca	Fe	K	Mg	Mn	Na	P	Si	Ti	Zr
Soil	Rio_Icacos (this study)	18.2817	-65.7903	5.09	0.28	3.18	<0.02	0.15	0.03	0.13	<0.02	32.9	0.28	231
	Guaba_Soil_1 (this study)	18.2818	-65.7905	4.46	0.16	2.26	0.31	0.16	0.03	0.1	<0.02	35.42	0.2	291
	Guaba_Soil_2 (this study)	18.2817	-65.7903	6.13	0.23	3.27	0.39	0.25	0.03	0.11	<0.02	30.53	0.25	273
	Chabaux *et al*., 2013			8.57	0.55	6.49	0.22	0.49	0.06	0.32	0.03	26.97	0.39	178
	White *et al*., 1998			8.06	0	3.13	0.63	0	0.01	0	0	30.91	0.26	163
	RI-1 (Riebe *et al*., 2003)			3.7	0.32	2.13	0.2	0.33	0.05	0.12	0.01	36.3	0.27	205
	RI-2 (Riebe *et al*., 2003)			4.5	0.37	2.83	0.05	0.35	0.05	0.1	0.01	33.9	0.44	264
	RI-4 (Riebe *et al*., 2003)			3.1	0.44	1.96	0.13	0.39	0.05	0.15	0.01	37.4	0.29	234
	RI-7 (Riebe *et al*., 2003)			3.6	0.5	2.37	0.19	0.44	0.05	0.15	0.01	35.9	0.29	230
Saprolite	Chabaux *et al*., 2013			9.29	0.53	6.68	0.24	0.59	0.06	0.28	0.02	27.75	0.41	182
	White *et al*., 1998			11.3	0	4.36	1.37	0.28	0.17	0	0	28.91	0.28	102
	RI-1 (Riebe *et al*., 2003)			6.6	0.22	4.23	0.24	0.63	0.05	0.08	0.01	28.1	0.39	171
	RI-2 (Riebe *et al*., 2003)			6.3	0.26	3.35	0.18	0.54	0.11	0.08	0.02	29.8	0.42	134
	RI-4 (Riebe *et al*., 2003)			6.5	0.22	3.42	0.27	0.63	0.15	0.1	0.01	29.1	0.43	115
	RI-7 (Riebe *et al*., 2003)			6.3	0.7	3.35	0.29	0.82	0.14	0.2	0.02	29	0.41	129

Rindlet	LGW1 (this study)	18.2811	-65.7891	9.13	4.65	4.57	0.98	1.53	0.13	2.37	0.06	28.77	0.29	125
	LGW2 (this study)	18.2939	-65.7917	9.53	5.22	5.14	0.68	1.77	0.13	2.29	0.06	27.49	0.29	132
	Buss *et al*., 2008			8.96	4.2	6.06	0.67	1.86	0.14	1.89	0.04	25.67	0.38	84
	Chabaux *et al*., 2013			9.42	4.25	5.62	0.62	1.81	0.14	2.19	0.07	27.57	0.36	111
Bedrock	LGW1 (this study)	18.2811	-65.7891	8.71	4.61	4.37	0.99	1.41	0.12	2.3	0.05	28.84	0.28	93
	LGW2 (this study)	18.2939	-65.7917	9.4	5.33	4.91	1.03	1.81	0.13	2.73	0.06	27.86	0.33	79
	Buss *et al*., 2008			8.99	5.16	5.92	0.71	1.74	0.13	2.21	0.05	25.84	0.35	85
	Chabaux *et al*., 2013			9.59	5.05	4.9	0.67	1.56	0.12	2.37	0.06	27.55	0.31	121
	White *et al*., 1998			9.1	5.17	4.76	0.77	1.31	0.14	2.49	0.06	28.61	0.29	60
Seep sediments	8/2/2016 (this study)	18.2852	-65.7900	7.53	3.55	4.45	0.52	1.41	0.11	1.66	0.03	30.06	0.28	76
	8/9/2016 (this study)	18.2852	-65.7900	6.74	3.24	4.52	0.48	1.43	0.11	1.46	0.03	31.16	0.29	69
	8/16/2016 (this study)	18.2852	-65.7900	7.5	3.42	4.37	0.44	1.4	0.11	1.59	0.02	30.33	0.28	80
	9/6/2016 (this study)	18.2852	-65.7900	6.65	2.72	4.83	0.44	1.56	0.12	1.18	0.03	29.05	0.34	83
	11/1/2016 (this study)	18.2852	-65.7900	5.4	2.47	4.25	0.42	1.51	0.11	1.02	0.02	32.48	0.3	74
	11/8/2016 (this study)	18.2852	-65.7900	5.68	2.48	4.67	0.44	1.54	0.11	1.02	0.02	31.41	0.32	79
	10/18/2016 (this study)	18.2852	-65.7900	5.59	2.46	4.4	0.38	1.52	0.12	1.02	0.02	32.91	0.3	75

Stream sediments	LS-1 Rio Icacos gage (this study, 2/25/2014)	18.2755	-65.7855	3.65	0.92	3.82	0.28	0.80	0.10	0.31	0.02	38.06	0.23	126
	LS-2 Rio Icacos gage (this study, 1/21/2015)	18.2755	-65.7855	4.26	0.69	3.53	0.35	0.73	0.09	0.25	<0.02	37.16	0.23	50
	LS-9 Rio Icacos gage (this study, 6/4/2014)	18.2755	-65.7855	4.28	1.50	4.27	0.34	0.80	0.10	0.65	0.03	36.35	0.21	60
	Rio Icacos gage (this study, averaged)	18.2755	-65.7855	4.06	1.04	3.87	0.32	0.77	0.1	0.4	0.02	37.19	0.22	79
	LS-3 Guaba gage (this study, 3/2/2014)	18.2819	-65.7885	4.46	1.64	5.75	0.65	0.85	0.10	0.85	0.02	34.77	0.24	106
	LS-11 Guaba gage (this study, 6/1/2014)	18.2819	-65.7885	4.34	1.40	4.19	0.70	0.86	0.09	0.76	0.02	35.92	0.22	94
	LS-4 Guaba gage (this study, 1/21/2015)	18.2819	-65.7885	4.58	1.76	4.77	0.78	1.08	0.11	0.87	0.02	35.45	0.25	79
	LS-13 Guaba gage (this study, 5/31/2016)	18.2819	-65.7885	4.93	1.82	5.53	0.69	0.85	0.10	0.98	0.03	34.81	0.23	123
	LS-10 Guaba gage (this study, 5/29/2015, bar)	18.2819	-65.7885	4.28	1.83	7.24	0.79	1.31	0.14	0.79	0.03	33.26	0.31	135
	Guaba gage (this study, averaged)	18.2819	-65.7885	4.52	1.69	5.5	0.72	0.99	0.11	0.85	0.02	34.84	0.25	107
	LS-6 (this study)	18.2904	-65.7883	5.17	0.4	4.63	0.54	0.75	0.24	0.14	0.02	35.31	0.3	89
	LS-7 (this study)	18.2709	-65.7841	3.19	0.93	4.23	0.25	0.66	0.09	0.35	0.03	37.79	0.22	76
	LS-8 (this study)	18.2702	-65.7839	3.73	0.87	4.55	0.3	0.69	0.11	0.37	0.03	36.47	0.22	135
	LS-12 (this study)	18.2691	-65.7833	3.83	0.89	4.32	0.34	0.75	0.09	0.33	0.02	36.93	0.26	155

Table S-5 Elemental compositions (atomic percentage) and elemental ratios (atom:atom) of plagioclase grains determined by SEM-EDS.

	Na	Al	Si	Ca	Na/Al	Si/Al	Ca/Al
Bedrock, LGW1 16-2, measured on 20190527							
spot 3	3.4	11.77	18.57	4.09	0.29	1.58	0.01
spot 4	5.2	9.97	20.39	2.24	0.52	2.05	0.02
spot 7	2.93	12.32	17.8	4.64	0.24	1.44	0.00
spot 8	3.6	11.67	18.68	3.91	0.31	1.60	0.01
spot 13	4.39	11.01	19.96	3.3	0.40	1.81	0.00
spot 14	3.77	11.43	19.35	3.77	0.33	1.69	0.00
spot 16	4.12	11.01	19.2	3.4	0.37	1.74	0.00
spot 17	3.8	11.53	18.57	3.8	0.33	1.61	0.00
spot 29	3.34	11.95	18.31	4.25	0.28	1.53	0.01
spot 35	3.83	11.56	18.64	3.75	0.33	1.61	0.01
spot 38	4.26	10.94	19.31	3.02	0.39	1.77	0.02
spot 44	3.15	12.08	18.32	4.2	0.26	1.52	0.00
spot 48	5.2	10.02	20.35	2.33	0.52	2.03	0.01
spot 60	1.69	13.02	16.50	5.71	0.13	1.27	0.00
spot 61	3.89	11.11	19.11	3.56	0.35	1.72	0.00
spot 62	2.61	12.72	17.25	4.96	0.21	1.36	0.00
spot 63	3.66	11.62	18.51	3.97	0.31	1.59	0.00
spot 64	1.98	13.16	16.31	5.47	0.15	1.24	0.00
spot 65	4.6	10.78	19.37	2.84	0.43	1.80	0.00
spot 66	4.11	11.47	19.2	3.6	0.36	1.67	0.00
spot 67	5.12	10.22	19.56	2.61	0.50	1.91	0.00
spot 68	3.61	11.45	18.66	4	0.32	1.63	0.00
spot 69	3.52	11.64	18.23	3.91	0.30	1.57	0.00
spot 80	0.48	14.42	15.37	6.92	0.03	1.07	0.00
spot 81	2.02	12.68	16.78	5.34	0.16	1.32	0.00
spot 82	2.74	12.74	17.41	4.72	0.22	1.37	0.00
spot 83	3.91	11.59	18.94	3.51	0.34	1.63	0.00
spot 84	3.02	11.88	17.88	4.37	0.25	1.51	0.01
spot 85	5.41	9.49	19.93	1.96	0.57	2.10	0.02
spot 99	4.22	10.92	18.91	3.31	0.39	1.73	0.02
spot 100	5.48	9.63	20.73	1.93	0.57	2.15	0.02
spot 101	5.64	9.41	21.02	1.56	0.60	2.23	0.02
Rindlet, LGW1 rindlet 1-10, measured on 20190523							
spot 3	3.79	10.96	17.53	3.79	0.35	1.60	0.35
spot 5	1.99	11.1	16.04	1.62	0.18	1.45	0.15
spot 6	2.77	11.79	16.24	3.75	0.23	1.38	0.32
spot 8	2.71	11.76	15.95	4.29	0.23	1.36	0.36
spot 10	3.1	11.22	18.15	3.71	0.28	1.62	0.33
spot 14	3.76	9.83	14.18	3.28	0.38	1.44	0.33
spot 16		17.61	11.29	0.37	0.00	0.64	0.02
spot 17	0.27	17.18	10.97	0.79	0.02	0.64	0.05

spot 18	3.66	11.27	18.19	3.85	0.32	1.61	0.34
spot 23	5.37	9.75	20.54	2.07	0.55	2.11	0.21
spot 24	4.67	10.43	19.69	2.77	0.45	1.89	0.27
spot 25		17.49	10.86	0.08	0.00	0.62	0.00
spot 26		17.97	11.24	0.26	0.00	0.63	0.01
spot 27	4.36	10.7	19.08	3.18	0.41	1.78	0.30
spot 29	1.32	13.95	15.82	6.59	0.09	1.13	0.47
spot 30	1.52	13.68	15.71	6.21	0.11	1.15	0.45
spot 31	4.19	10.93	19.08	3.36	0.38	1.75	0.31
spot 32		18.94	10.88	0.12	0.00	0.57	0.01
spot 33	1.21	13.18	14.61	1.46	0.09	1.11	0.11
Rindlet, RC-5 (Chabaux *et al*., 2013), measured on 20190602							
spot 15	4.46	10.26	20.11	2.81	0.43	1.96	0.27
spot 16	4.17	10.77	19.64	3.07	0.39	1.82	0.29
spot 17	3.31	11.31	18.2	4.08	0.29	1.61	0.36
spot 18	3.27	11.86	17.42	2.76	0.28	1.47	0.23
spot 19	2.07	14.78	18.13	3.3	0.14	1.23	0.22
spot 20	2.34	13.44	17.42	3.87	0.17	1.30	0.29
spot 21	3.44	11.77	18.74	4.21	0.29	1.59	0.36
spot 22	5.09	10.12	20.71	2.5	0.50	2.05	0.25
spot 23	3.54	11.25	17.49	3.64	0.31	1.55	0.32
Rindlet, LGW1 rindlet 1-10, measured on 20190623							
spot 24	3.44	10.17	16.54	2.59	0.34	1.63	0.25
spot 25	4.17	9.54	18.01	2.39	0.44	1.89	0.25
spot 26	2.24	11.31	13.93	1.74	0.20	1.23	0.15
spot 27	2.22	10.94	14.01	2.15	0.20	1.28	0.20
spot 28	2.67	10.83	14.57	2.67	0.25	1.35	0.25
spot 29	2.85	11.12	16.2	3.61	0.26	1.46	0.32
spot 39	3.44	10.46	17.36	3.51	0.33	1.66	0.34
spot 40	5.77	10.4	23.25	2.04	0.55	2.24	0.20
spot 41	4.18	9.06	17.81	2.45	0.46	1.97	0.27
spot 42		17.9	12.47	0.25	0.00	0.70	0.01
spot 43		17.78	12.54	0.26	0.00	0.71	0.01
spot 47	0.43	14.02	9.61	0.58	0.03	0.69	0.04
spot 48	0.68	14.06	11.5	1.24	0.05	0.82	0.09
spot 49	5.03	8.7	19.41	1.72	0.58	2.23	0.20
spot 35	2.99	10.84	16.69	3.87	0.28	1.54	0.36
spot 36	3.31	10.28	16.9	3.24	0.32	1.64	0.32
spot 37	2.08	11.02	14.68	2.44	0.19	1.33	0.22
spot 38	2	11.04	14.35	2.75	0.18	1.30	0.25
Rindlet, LGW1 rindlet 1-20, measured on 20190804							
spot 47	3.32	11.74	17.64	4.16	0.28	1.50	0.35
spot 48	3.37	12.06	18.69	3.77	0.28	1.55	0.31
spot 49	4.6	10.92	20.57	2.98	0.42	1.88	0.27
spot 50	4.7	10.64	20.44	2.81	0.44	1.92	0.26
spot 66	3.44	11.39	18.47	3.98	0.30	1.62	0.35

spot 67	4.64	10.8	20.5	2.93	0.43	1.90	0.27
spot 73	4.42	11.12	20.01	3.1	0.40	1.80	0.28
Rindlet, LGW1 rindlet 1-20, measured on 20200802							
spot 1	0.17	10.8	9.69		0.02	0.90	0.00
spot 2	1.27	9.14	9.76	0.32	0.14	1.07	0.04
spot 3	3.43	8.47	14.45	2.51	0.40	1.71	0.30
spot 5	3.43	7.89	13.52	2.19	0.43	1.71	0.28
spot 7	3.34	7.84	13.43	2.26	0.43	1.71	0.29
Seep sediment (epoxy-1), collected during Aug 2–9, 2016 (0.85–2.56 mm size fraction), measured on 20190804							
spot 11	0.19	7.21	8.88	0.56	0.03	1.23	0.08
spot 13	2.69	6.61	11.01	1.87	0.41	1.67	0.28
spot 16	2.37	7.81	11.57	2.57	0.30	1.48	0.33
spot 18	1.94	5.63	9.89	1.93	0.34	1.76	0.34
spot 19	2.81	8.87	13.81	2.02	0.32	1.56	0.23
spot 20	3.9	11.09	18.08	3.37	0.35	1.63	0.30
spot 23	2.51	5.81	9.89	1.59	0.43	1.70	0.27
spot 24	2.3	6.53	10.12	1.96	0.35	1.55	0.30
spot 25	1.26	3.67	5.42	1.05	0.34	1.48	0.29
spot 30	1.17	4.7	6.23	1.47	0.25	1.33	0.31
spot 40	1.87	5.24	7.92	1.49	0.36	1.51	0.28
spot 43	2.24	6.45	10.02	1.96	0.35	1.55	0.30
spot 44	2.51	5.56	9.52	1.38	0.45	1.71	0.25
spot 45	1.49	3.29	5.39	0.71	0.45	1.64	0.22
spot 46		9.12	9.23		0.00	1.01	0.00
spot 48	1.47	4.08	6.09	1.09	0.36	1.49	0.27
spot 49	0.75	4.15	6.82	0.61	0.18	1.64	0.15
spot 57		7.17	6.47	0.02	0.00	0.90	0.00
spot 58		6.37	5.72	0.05	0.00	0.90	0.01
spot 60	1.19	5.75	6.79	1.29	0.21	1.18	0.22
spot 64	0.12	6.51	3.43		0.02	0.53	0.00
spot 65	0.04	4.71	2.54	0.06	0.01	0.54	0.01
spot 66	0.18	6.22	3.77	0.12	0.03	0.61	0.02
spot 67	3.7	11.27	17.92	3.56	0.33	1.59	0.32
spot 68	3.8	10.96	17.71	3.3	0.35	1.62	0.30
spot 69	3.61	11.38	17.82	3.68	0.32	1.57	0.32
spot 70	0.82	3.54	4.27	0.74	0.23	1.21	0.21
spot 71	3.09	11.76	17.15	3.9	0.26	1.46	0.33
spot 72	1.75	6.01	8.52	1.86	0.29	1.42	0.31
spot 81	1.96	6.24	9.14	1.94	0.31	1.46	0.31
Seep sediment (epoxy-2), collected during Aug 9–16, 2016 (0.85–2.56 mm size fraction), measured on 20190820							
spot 10	5.28	9.63	18.43	2	0.55	1.91	0.21
spot 19	5.55	9.21	18.48	1.67	0.60	2.01	0.18
spot 23	3.86	11.01	17.36	3.02	0.35	1.58	0.27
spot 26	3.46	9.25	14.55	2.52	0.37	1.57	0.27
spot 32	1.58	4	7.23	1.02	0.40	1.81	0.26

spot 37	1.28	3.91	5.79	0.69	0.33	1.48	0.18
spot 40	0.67	3.4	3.66	0.4	0.20	1.08	0.12
spot 48	1.36	4.82	6.48	1.26	0.28	1.34	0.26
spot 74	1.34	4.63	6.71	0.31	0.29	1.45	0.07
spot 88		0.58	0.59	0.02	0.00	1.02	0.03
spot 89		0.63	0.74	0.02	0.00	1.17	0.03
spot 90		0.55	0.66		0.00	1.20	0.00
spot 91		0.69	0.79	0.02	0.00	1.14	0.03
spot 92		0.46	0.47		0.00	1.02	0.00
spot 97		9.01	7.97		0.00	0.88	0.00
spot 98	0.12	4.52	3.92	0.05	0.03	0.87	0.01
spot 99		7.78	6.56		0.00	0.84	0.00
spot 100		2.93	2.25	0.02	0.00	0.77	0.01
spot 101		5.15	4.3	0.03	0.00	0.83	0.01
spot 102		6.76	5.71		0.00	0.84	0.00
spot 103	4.61	9.7	16.58	2.1	0.48	1.71	0.22
spot 104	5.16	9.21	16.88	1.73	0.56	1.83	0.19
spot 105	2.8	7.81	11.42	2.01	0.36	1.46	0.26
Seep sediment (epoxy-3), collected during Aug 26– Sep 02, 2016 (0.85–2.56 mm size fraction), measured on 20190805							
spot 21	1.31	4.16	6.45	1.4	0.31	1.55	0.34
spot 22	3.33	11.95	18.66	4.24	0.28	1.56	0.35
spot 23	4.7	10.41	20.2	2.6	0.45	1.94	0.25
spot 26	4.94	10.67	20.97	2.74	0.46	1.97	0.26
Seep sediment (epoxy-5), collected during Sep 13– Sep 20, 2016 (0.85–2.56 mm size fraction), measured on 20190802							
spot 5	4.85	9.72	20.31	2.1	0.50	2.09	0.22
spot 7	1.5	3.94	8	0.92	0.38	2.03	0.23
spot 8	0.95	3.74	6.18	1.24	0.25	1.65	0.33
spot 9	1.65	6.02	9.49	2.15	0.27	1.58	0.36
spot 10	2.21	6.5	12.89	1.44	0.34	1.98	0.22
spot 11	1.9	5.19	9.5	1.48	0.37	1.83	0.29
spot 14	4.07	11.06	19.86	3.26	0.37	1.80	0.29
spot 16	4.23	10.57	20.28	3.13	0.40	1.92	0.30
spot 25	3.86	11.33	19.91	3.46	0.34	1.76	0.31
spot 26	1.51	7.19	10.18	1.8	0.21	1.42	0.25
spot 29	1.42	6.23	9.17	2.29	0.23	1.47	0.37
spot 35	5.03	9.99	20.98	2.19	0.50	2.10	0.22

Table S-6 Concentrations (µM) of major cations, dissolved silica and anions of the seep water and surface water from Quebrada Guaba (sampled at the gage). BDL: below detection limit.

Sample ID	Al	Ba	Ca	Fe	K	Mg	Mn	Na	P	Si	Sr	Cl^-	SO_4^{2-}	NO_3^-	Sample date
Seep															
R191seep	BDL	0.07	86	BDL	10	31	BDL	265	BDL	395	0.2	216	12	3	7/7/2012
PR13-33	BDL	0.06	97	0.1	11	35	BDL	285	BDL	417	0.23	206	9	BDL	3/24/2013
PR13-56	0.7	0.05	79	0.1	8	32	BDL	247	BDL	328	0.19	185	10	BDL	3/30/2013
PR13-77	0.5	0.06	81	0.1	8	33	BDL	242	BDL	290	0.19	183	9	BDL	3/31/2013
PR14-13	1.6	0.07	89	14.1	11	40	1.9	257	BDL	336	0.24	198	29	87	2/23/2014
PR14-44	BDL	0.07	88	BDL	11	32	BDL	272	BDL	389	0.24	232	39	BDL	2/26/2014
PR14-67	BDL	0.08	89	BDL	12	32	BDL	268	BDL	390	0.24	190	13	BDL	3/2/2014
PR14-76	0.6	0.06	91	BDL	12	32	BDL	274	BDL	381	0.19	194	12	1	6/1/2014
PR14-85	BDL	0.07	93	BDL	11	32	BDL	279	BDL	438	0.19	198	12	2	6/4/2014
PR15-13	0.3	0.07	94	BDL	9	33	BDL	273	BDL	406	0.21	192	11	1	1/20/2015
PR15-48	0.5	0.07	94	BDL	7	34	BDL	268	BDL	407	0.21	189	10	BDL	1/23/2015
PR15-59	0.3	0.07	99	BDL	6	35	BDL	277	BDL	416	0.22	192	10	BDL	1/24/2015
PR15-102	0.3	0.07	97	BDL	5	34	BDL	269	BDL	402	0.22	195	11	1	1/28/2015
PR15-145	3.3	0.08	82	1.5	16	29	BDL	232	1	425	0.21	195	15	BDL	5/26/2015
PR15-203	BDL	0.09	96	BDL	9	35	BDL	242	1.6	384	0.24	174	10	BDL	2/24/2015
PR15-205	0.2	0.07	86	BDL	8	31	BDL	251	BDL	403	0.21	183	11	BDL	3/31/2015
PR15-212	BDL	0.07	88	BDL	9	32	BDL	248	128	416	0.22	190			4/29/2015
PR15-224	0.3	0.06	88	BDL	7	32	BDL	247	0.22	390	0.21	177	13	BDL	9/30/2015
PR15-228	BDL	0.07	87	0.1	10	32	BDL	248	0.4	405	0.21	129	6	BDL	10/28/2015
PR15-235	BDL	0.07	96	BDL	10	34	BDL	253	1.64	386	0.21	190	11	10	12/1/2015
PR16-21	BDL	0.07	80	BDL	8	30	BDL	239	2.02	339	0.18	189	16	7	6/1/2016
PR16-24	BDL	0.06	70	BDL	7	27	BDL	231	0.84	282	0.17	184	17	7	6/2/2016
LCZO-7	BDL	0.06	80	BDL	8	31	BDL	241	BDL	334	0.18	191	18	7	6/3/2016
LCZO-16	0.01	0.07	84	BDL	8	31	BDL	231	BDL	348	0.2	179	9	9	6/4/2016
LCZO-25	BDL	0.05	78	BDL	8	30	BDL	245	BDL	376	0.19				7/19/2016

LCZO-30	0.3	0.05	72	BDL	7	28	BDL	221	BDL	332	0.17				7/26/2016
LCZO-32	BDL	0.06	83	BDL	8	32	BDL	250	BDL	376	0.2				8/2/2016
LCZO-40	BDL	0.06	84	BDL	8	32	BDL	250	BDL	368	0.2				8/9/2016
LCZO-41	BDL	0.06	84	BDL	8	32	BDL	247	BDL	376	0.2				8/10/2016
LCZO-46	BDL	0.06	77	BDL	7	30	BDL	232	BDL	366	0.19				8/16/2016
LCZO-51	BDL	BDL	52	BDL	2	10	BDL		BDL	337	0.1				8/26/2016
LCZO-56	BDL	0.05	75	BDL	7	27	BDL	219	BDL	357	0.16				9/2/2016
LCZO-61	BDL	0.05	78	BDL	8	28	BDL	221	BDL	376	0.17				9/6/2016
LCZO-66	BDL	0.05	76	BDL	8	28	BDL	219	BDL	379	0.17				9/13/2016
LCZO-71	BDL	0.05	80	BDL	8	29	BDL	227	BDL	379	0.18				9/20/2016
LCZO-76	BDL	0.05	79	BDL	8	29	BDL	231	BDL	381	0.18				9/27/2016
LCZO-81	BDL	0.05	71	BDL	7	26	BDL	209	BDL	375	0.16				10/4/2016
LCZO-86	BDL	0.05	82	BDL	8	30	BDL	238	BDL	383	0.19				10/11/2016
Mean conc.	-	0.06	84	-	8	31	-	247	-	375	0.2	190	14	-	
Standard derivation	-	0.01	9	-	2	4	-	19	-	35	0.03	18	7	-	
Quebrada Guaba															
PR16-5	0.7	BDL	49	0.6	11	32	BDL	178	BDL	218	0.09				5/31/2016
PR16-22	2.2	BDL	33	0.9	10	23	BDL	139	BDL	116	0.06				6/2/2016
LCZO-05	0.5	0.04	50	0.5	11	32	BDL	186	BDL	215	0.1				6/3/2016
LCZO-14	0.4	0.04	54	0.5	11	35	BDL	199	BDL	246	0.11				6/4/2016
LCZO-22	0.4	BDL	59	0.3	10	37	BDL	190	BDL	280	0.13				7/19/2016
LCZO-26	1.5	BDL	BDL	0.6	11	27	BDL	135	BDL	131	0.09				7/26/2016
LCZO-33	0.6	0.04	59	0.3	11	39	BDL	189	BDL	267	0.13				8/2/2016
LCZO-38	0.4	BDL	56	0.3	10	37	BDL	184	BDL	282	0.12				8/9/2016
LCZO-43	0.9	BDL	52	0.8	11	35	BDL	169	BDL	230	0.12				8/10/2016
LCZO-48	0.5	BDL!	53	0.3	9	35	BDL	173	BDL	266	0.12				8/16/2016
LCZO-53	0.8	BDL	60	0.9	11	36	BDL	173	BDL	234	0.12				8/26/2016
LCZO-58	2	BDL	31	1.3	12	22	BDL	119	BDL	123	0.06				9/2/2016
LCZO-63	0.5	BDL	50	0.7	12	31	BDL	165	BDL	212	0.1				9/6/2016

LCZO-68	BDL	0.04	58	0.6	10	35	BDL	177	BDL	267	0.12				9/13/2016
LCZO-73	BDL	BDL	58	0.5	10	36	BDL	181	BDL	289	0.12				9/20/2016
LCZO-78	0.3	BDL	59	0.5	10	37	BDL	184	BDL	302	0.12				9/27/2016
LCZO-83	BDL	BDL	52	0.4	11	32	BDL	166	BDL	234	0.11				10/4/2016
LCZO-88	BDL	BDL	58	0.3	10	36	BDL	182	BDL	282	0.12				10/11/2016
Mean conc.	0.8	-	52	0.6	11	33	-	172	-	233	0.11				
Standard derivation	0.6	-	9	0.3	1	5	-	20	-	56	0.02				

Supplementary Figures

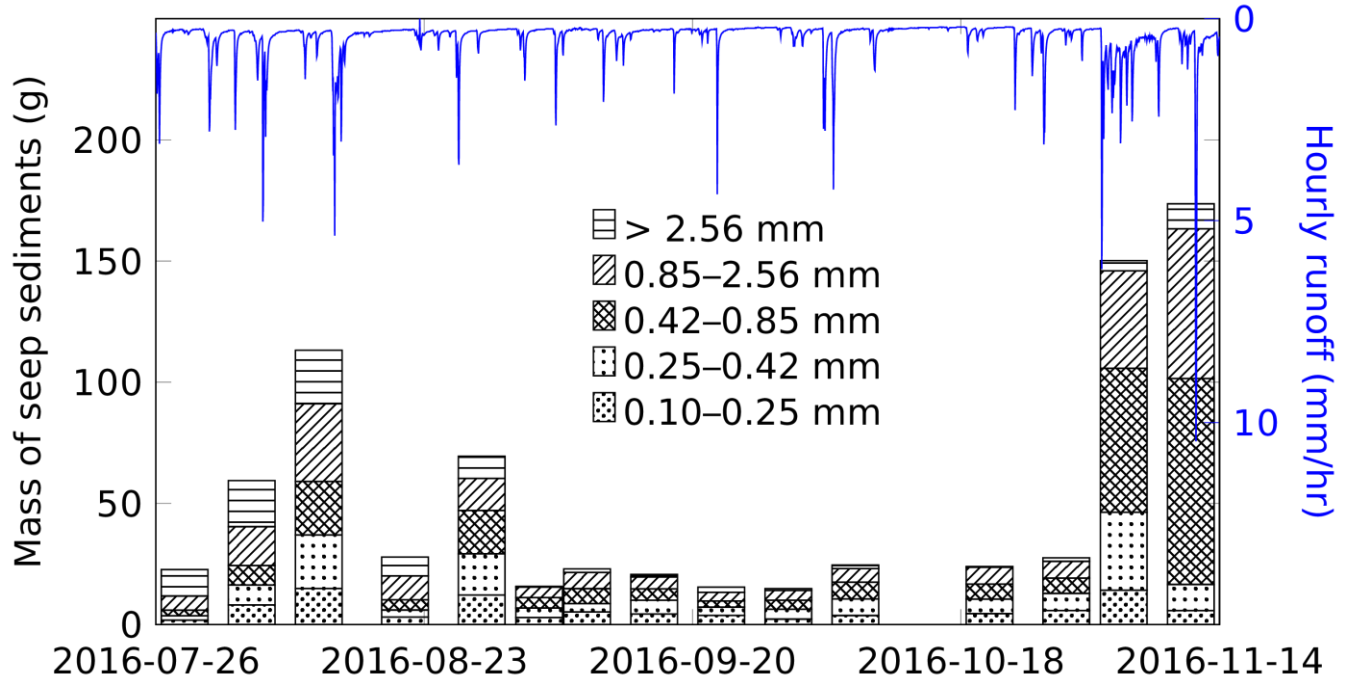

Figure S-1 Hourly runoff measured at Río Icacos gage (USGS station: 50075000) and weekly yield of seep sediments collected from a seep (see Fig. 1a for location). The bar chart shows the abundance of different size fractions of the seep sediments.

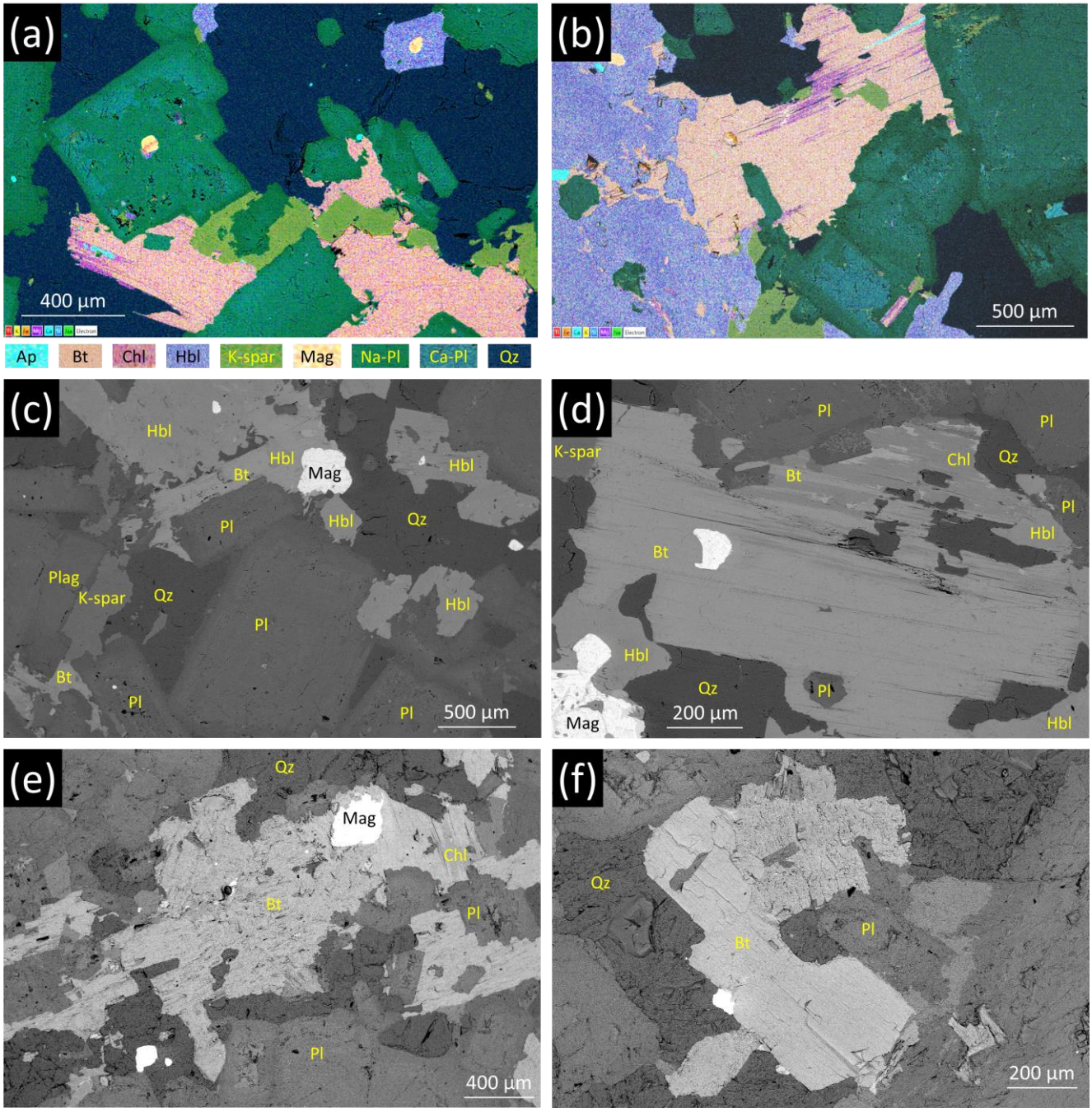

Figure S-2 Elemental maps **(a, b)** and BSE images **(c-f)** of an unweathered corestone from the bottom of borehole LGW1 at ~28.3 mbls (LGW1 16, **a-d**) and the interior of a rindlet sample from borehole LGW1 at 5.38–5.40 mbls (LGW1 1-20, **e, f**). Ap: apatite, Bt: biotite, Chl: chlorite, Hbl: hornblende, Kln: kaolinite, K-spar: K-feldspar, Mag: magnetite, Pl: plagioclase, Qz: quartz.

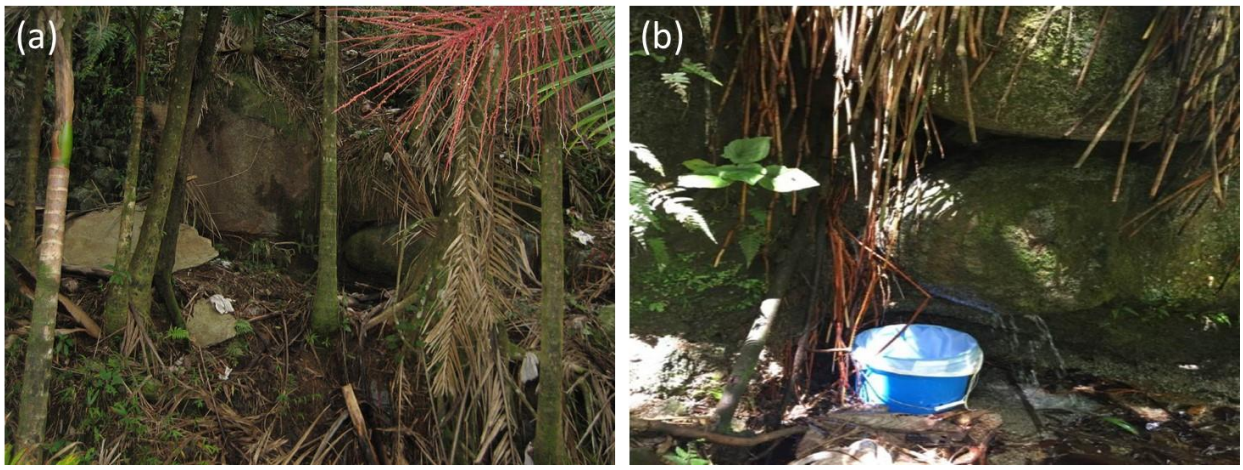

Figure S-3 Zoom-out **(a)** and Zoom-in **(b)** images of the sampling site of seep sediments. The bucket with a filter bag (100 µm filter size) was used to collect seep sediments.

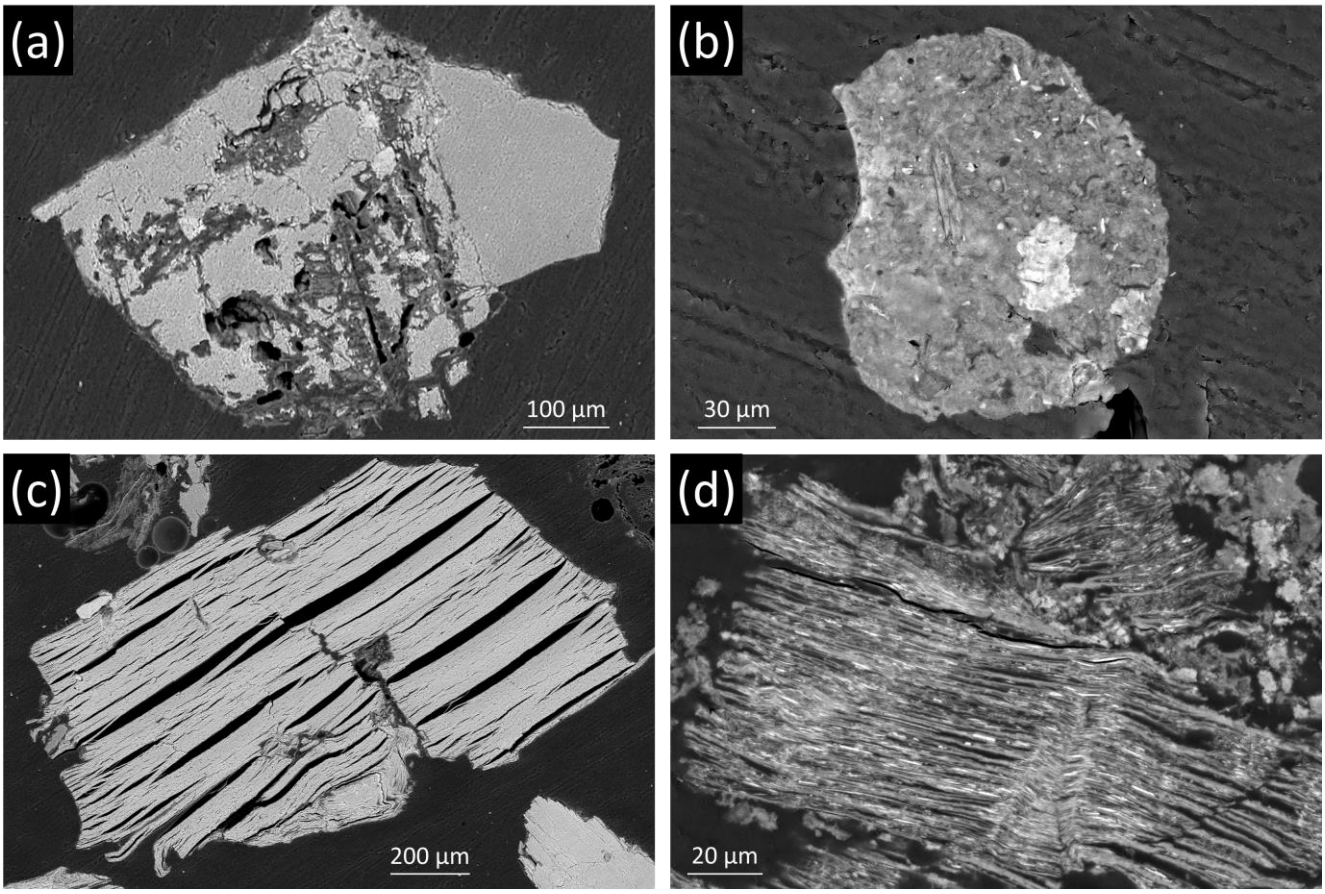

Figure S-4 BSE images of seep sediments collected during Aug 9–16, 2016 (0.85–2.56 mm size fraction). **(a)** slight weathered and fractured plagioclase, **(b)** higher weathered plagioclase (the elemental compositions are between kaolinite and gibbsite), **(c)** exfoliated and weathered biotite, **(d)** highly weathered biotite (the elemental compositions are between vermiculite and kaolinite).

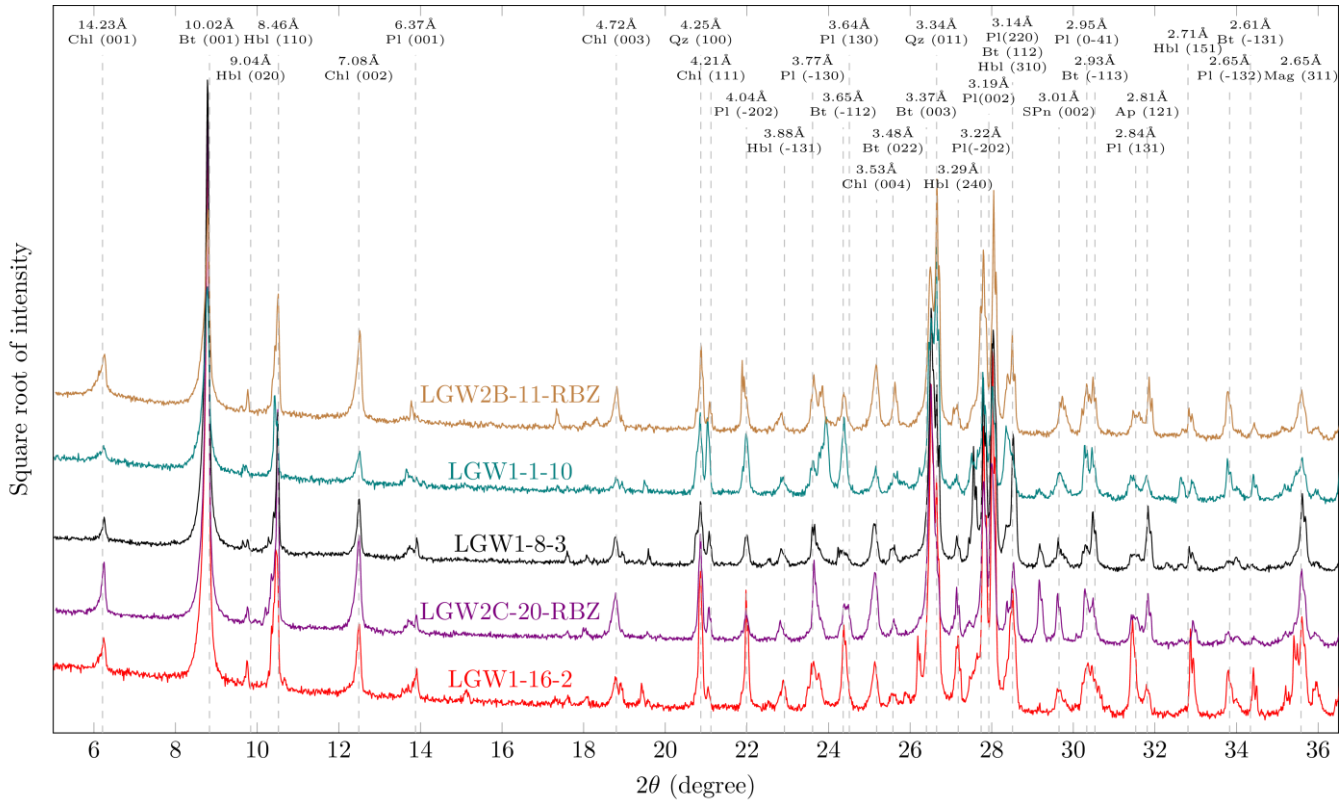

Figure S-5 Powder XRD patterns of corestone (bottom three) and rindlet samples (top two) from two boreholes at Río Icacos. The 2θ values were converted to Cu-$K\alpha$ radiation for conventional comparisons. The XRD patterns were compared to the patterns of well characterized minerals (dashed lines) which are available on the RRUFF Project (https://rruff.info/). Ap: apatite, Bt: biotite, Chl: chlorite, Hbl: hornblende, Mag: magnetite, Pl: plagioclase, Qz: quartz, Spn: sphene.

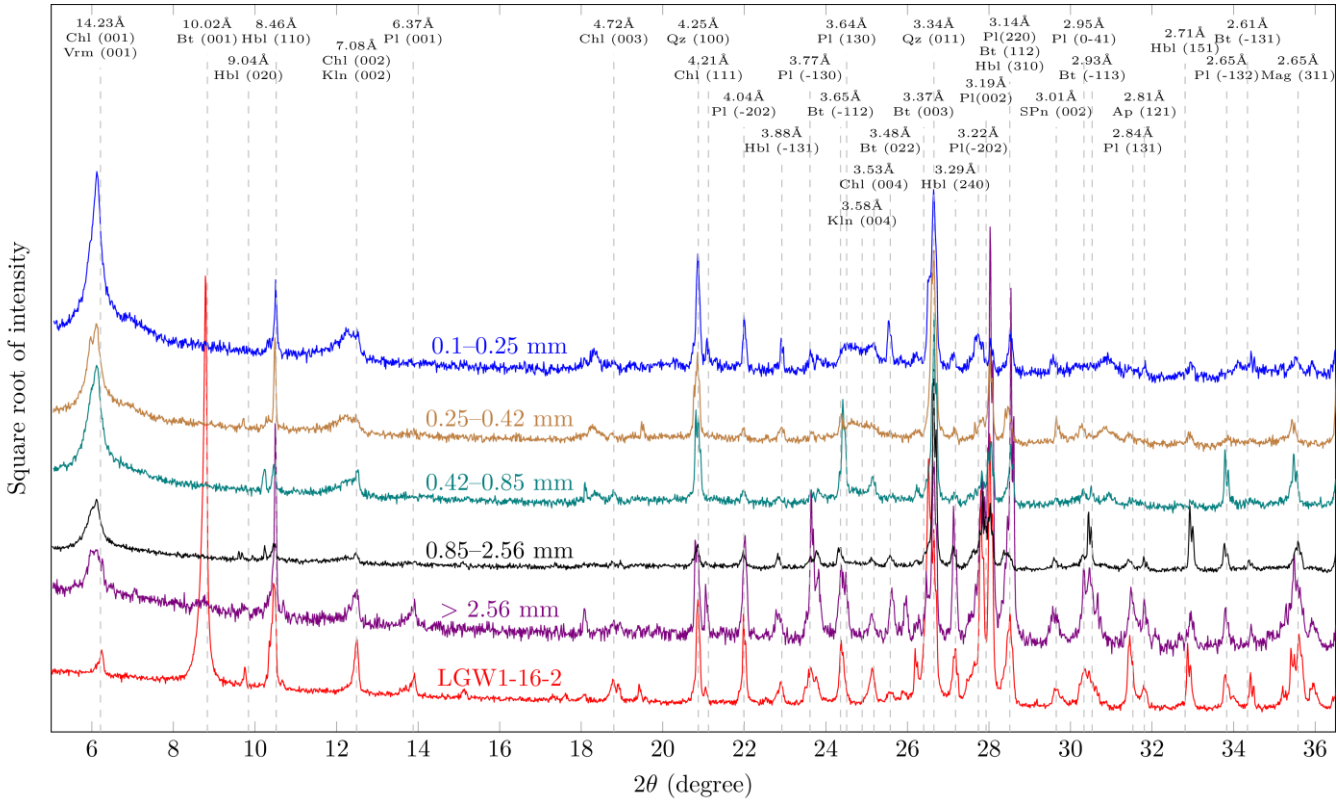

Figure S-6 Powder XRD patterns of seep sediments with different sizes. The samples were collected during Aug 2–7, 2016 at Río Icacos. The bottom line represents a corestone sample for comparison. Ap: apatite, Bt: biotite, Chl: chlorite, Hbl: hornblende, Kln: kaolinite, Mag: magnetite, Pl: plagioclase, Qz: quartz, Spn: sphene, Vrm: vermiculite.

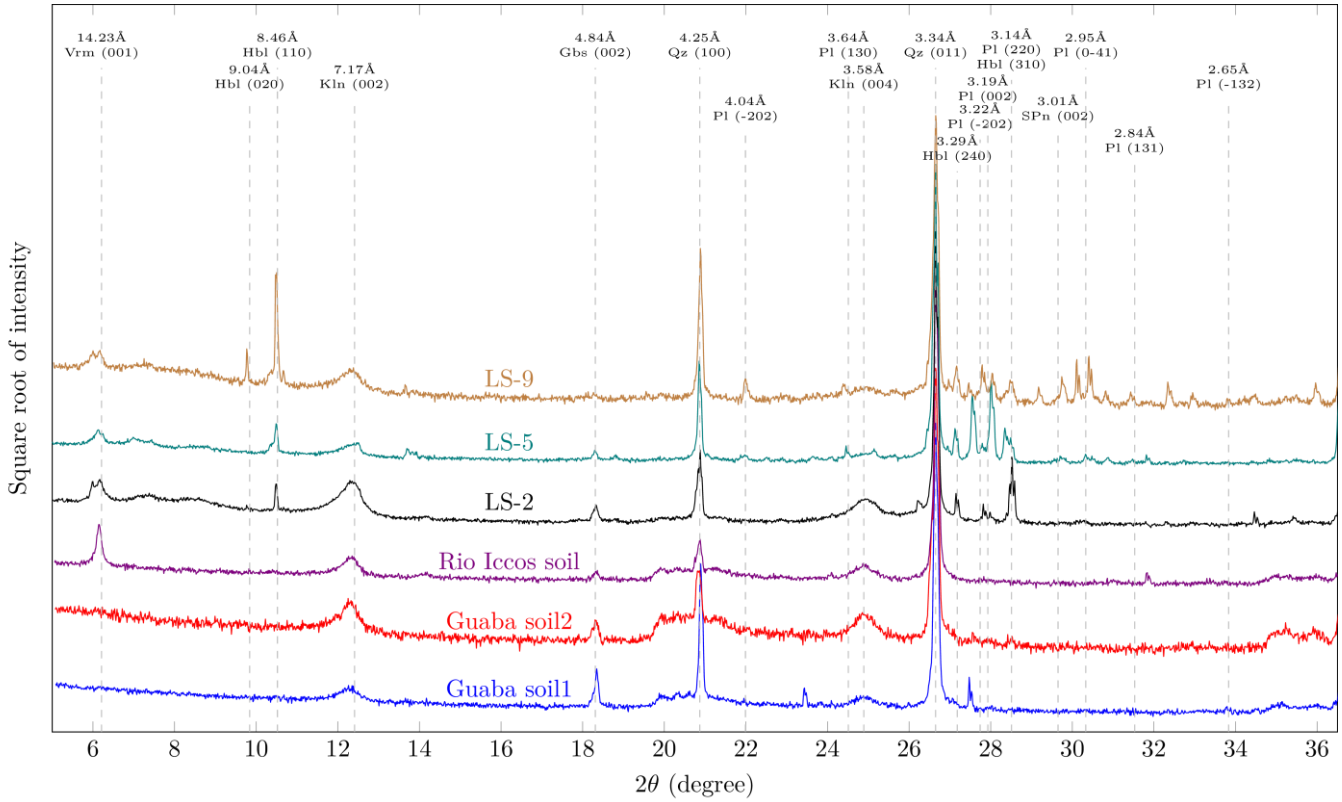

Figure S-7 Powder XRD patterns of soil (bottom three) and stream sediments (top three) collected at Río Icacos. Note that plagioclase and hornblende are only present in stream sediments but not in soils. Gbs: gibbsite, Hbl: hornblende, Kln: kaolinite, Pl: plagioclase, Qz: quartz, Spn: sphene, Vrm: vermiculite.

Supplementary Information References

Bhatt, M.P., McDowell, W.H. (2007) Controls on major solutes within the drainage network of a rapidly weathering tropical watershed. *Water Resources Research* 43, W11402.

Brantley, S.L., Buss, H., Lebedeva, M., Fletcher, R.C., Ma, L. (2011) Investigating the complex interface where bedrock transforms to regolith. *Applied Geochemistry* 26, S12–S15.

Brocard, G.Y., Willenbring, J.K., Scatena, F.N., Johnson, A.H. (2015) Effects of a tectonically-triggered wave of incision on riverine exports and soil mineralogy in the Luquillo Mountains of Puerto Rico. *Applied Geochemistry* 63, 586–598.

Brown, S.R. (1987) Fluid flow through rock joints: The effect of surface roughness. *Journal of Geophysical Research* 92, 1337–1347.

Buss, H.L., Sak, P.B., Webb, S.M., Brantley, S.L. (2008) Weathering of the Rio Blanco quartz diorite, Luquillo Mountains, Puerto Rico: Coupling oxidation, dissolution, and fracturing. *Geochimica et Cosmochimica Acta* 72, 4488–4507.

Buss, H.L., Chapela Lara, M., Moore, O.W., Kurtz, A.C., Schulz, M.S., White, A.F. (2017) Lithological influences on contemporary and long-term regolith weathering at the Luquillo Critical Zone Observatory. *Geochimica et Cosmochimica Acta* 196, 224–251.

Chabaux, F., Blaes, E., Stille, P., Roupert, R.D., Pelt, E., Dosseto, A., Ma, L., Buss, H.L., Brantley, S.L. (2013) Regolith formation rate from U-series nuclides: Implications from the study of a spheroidal weathering profile in the Rio Icacos watershed (Puerto Rico). *Geochimica et Cosmochimica Acta* 100, 73–95.

Comas, X., Wright, W., Hynek, S.A., Fletcher, R.C., Brantley, S.L. (2019) Understanding fracture distribution and its relation to knickpoint evolution in the Rio Icacos watershed (Luquillo Critical Zone Observatory, Puerto Rico) using landscape-scale hydrogeophysics. *Earth Surface Processes and Landforms* 44, 877–885.

Eberl D.D. (2003) User's guide to RockJock-a program for determining quantitative mineralogy from powder X-ray diffraction data. U.S. Geological Survey, Open-file report 03–78.

Ferrier, K.L., Kirchner, J.W., Riebe, C.S., Finkel, R.C. (2010) Mineral-specific chemical weathering rates over millennial timescales: Measurements at Rio Icacos, Puerto Rico. *Chemical Geology* 277, 101–114.

Fletcher, R.C., Buss, H.L., Brantley, S.L. (2006) A spheroidal weathering model coupling porewater chemistry to soil thicknesses during steady-state denudation. *Earth and Planetary Science Letters* 244, 444–457.

Freeze, R.A., Cherry, J.A. (1979) *Groundwater*. Prentice-Hall, Englewood Cliffs, New Jersey.

Hynek, S., Comas, X., Brantley, S.L. (2017) The effect of fractures on weathering of igneous and volcaniclastic sedimentary rocks in the Puerto Rican tropical rain forest. *15th Water-rock Interaction International Symposium, Wri-15*, 972–975.

McDowell, W.H., Bowden, W.B., Asbury, C.E. (1992) Riparian nitrogen dynamics in two geomorphologically distinct tropical rain forest watersheds: subsurface solute patterns. *Biogeochemistry* 18, 53–75.

Murphy, S.F., Brantley, S.L., Blum, A.E., White, A.F., Dong, H.L. (1998) Chemical weathering in a tropical watershed, Luquillo mountains, Puerto Rico: II. Rate and mechanism of biotite weathering. *Geochimica et Cosmochimica Acta* 62, 227–243.

Navarre-Sitchler, A.K., Cole, D.R., Rother, G., Jin, L.X., Buss, H.L., Brantley, S.L. (2013) Porosity and surface area evolution during weathering of two igneous rocks. *Geochimica et Cosmochimica Acta* 109, 400–413.

Orlando, J. (2014) The anatomy of weathering profiles on different lithologies in the tropical forest of northeastern Puerto Rico: from bedrock to clouds. Master thesis: Pennsylvania State University.

Orlando, J., Comas, X., Hynek, S.A., Buss, H.L., Brantley, S.L. (2016) Architecture of the deep critical zone in the Río Icacos watershed (Luquillo Critical Zone Observatory, Puerto Rico) inferred from drilling and ground penetrating radar (GPR). *Earth Surface Processes and Landforms* 41, 1826–1840.

Riebe, C.S., Kirchner, J.W., Finkel, R.C. (2003) Long-term rates of chemical weathering and physical erosion from cosmogenic nuclides and geochemical mass balance. *Geochimica et Cosmochimica Acta* 67, 4411–4427.

Saraceno, J.F., Shanley, J.B., Downing, B.D., Pellerin, B.A. (2017) Clearing the waters: Evaluating the need for site-specific field fluorescence corrections based on turbidity measurements. *Limnology and Oceanography: Methods* 15, 408–416.

Schulz, M.S., White, A.F. (1999) Chemical weathering in a tropical watershed, Luquillo mountains, Puerto Rico III: Quartz dissolution rates. *Geochimica et Cosmochimica Acta* 63, 337–350.

Shanley, J.B., McDowell, W.H., Stallard, R.F. (2011) Long-term patterns and short-term dynamics of stream solutes and suspended sediment in a rapidly weathering tropical watershed. *Water Resources Research* 47, W07515.

Snow, D.T. (1969) Anisotropic permeability of fractured media. *Water Resources Research* 5, 1273–1289.

Thompson, A., Rancourt, D.G., Chadwick, O.A., Chorover, J. (2011) Iron solid-phase differentiation along a redox gradient in basaltic soils. *Geochimica et Cosmochimica Acta* 75, 119–133.

Turner, B.F., Stallard, R.F., Brantley, S.L. (2003) Investigation of in situ weathering of quartz diorite bedrock in the Rio Icacos basin, Luquillo Experimental Forest, Puerto Rico. *Chemical Geology* 202, 313–341.

White, A.F., Blum, A.E., Schulz, M.S., Vivit, D.V., Stonestrom, D.A., Larsen, M., Murphy, S.F., Eberl, D. (1998) Chemical weathering in a tropical watershed, Luquillo mountains, Puerto Rico: I. Long-term versus short-term weathering fluxes. *Geochimica et Cosmochimica Acta* 62, 209–226.